IN-34
194092
40 P

NASA Technical Memorandum 106369
ICOMP–93–36; CMOTT–93–13

Multigrid Direct Numerical Simulation of the Whole Process of Flow Transition in 3–D Boundary Layers

Chaoqun Liu
Institute for Computational Mechanics in Propulsion
and Center for Modeling of Turbulence and Transition
Lewis Research Center
Cleveland, Ohio

and University of Colorado at Denver
Denver, Colorado

and

Zhining Liu
University of Colorado at Denver
Denver, Colorado

N94-17557
Unclas
G3/34 0194092

(NASA-TM-106369) MULTIGRID DIRECT NUMERICAL SIMULATION OF THE WHOLE PROCESS OF FLOW TRANSITION IN 3-D BOUNDARY LAYERS (NASA) 40 p

November 1993

INSTITUTE FOR COMPUTATIONAL MECHANICS IN PROPULSION
NASA
ICOMP
Lewis Research Center
Ohio Aerospace Institute

NASA

Multigrid Direct Numerical Simulation of the Whole Process of Flow Transition in 3-D Boundary Layers

Chaoqun Liu
Institute for Computational Mechanics in Propulsion
and Center for Modeling of Turbulence and Transition
Lewis Research Center
Cleveland, Ohio 44135
and University of Colorado at Denver
Denver, Colorado 80217

and

Zhining Liu
University of Colorado at Denver
Denver, Colorado 80217

Abstract

A new technology was developed in this study which provides a successful numerical simulation of the whole process of flow transition in 3-D boundary layers, including linear growth, secondary instability, breakdown, and transition at relatively low CPU cost. Most other spatial numerical simulations require high CPU cost and blow up at the stage of flow breakdown. A fourth-order finite difference scheme on stretched and staggered grids, a fully implicit time-marching technique, a semi-coarsening multigrid based on the so-called approximate line-box relaxation, and a buffer domain for the outflow boundary conditions were all used for high-order accuracy, good stability, and fast convergence. A new fine-coarse-fine grid mapping technique was developed to keep the code running after the laminar flow breaks down. The computational results are in good agreement with linear stability theory, secondary instability theory, and some experiments. The cost for a typical case with $162 \times 34 \times 34$ grid is around 2 CRAY-YMP CPU hours for 10 T-S periods.

1 Introduction

The transition process from laminar to turbulent flow in a wall-bounded shear flow is still a challenging and unsolved problem. Natural transition is a multi-stage process (Narasimha, 1990) involving 2-D linear evolution, 3-D secondary instability, breakdown, and transition (Figure 1).

The linear stability equation was established by Orr (1907a, b) and Sommerfeld (1908), was solved by Tollmien (1931) and Schlichting (1932), and was experimentally confirmed by Schubauer and Skramstad (1948). The secondary instability was observed by Klebanoff, Tidstrom & Sargent (1962) for K-type fundamental transition, and was observed by Kachanov, Kozlov and Levchenko (1978) for subharmonic transition. The theoretical work was accomplished by Herbert (1983a & 1983b). There is really very little work, either theoretical or experimental, about the breakdown and transition zones which are the major parts of transition process.

The numerical study of transition is still quite limited due to the lack of computational resources. First, most numerical studies are temporal (Orszag & Kells, 1980; Wray & Hussaini, 1984; Kleiser & Laurien, 1985; Zang & Hussaini, 1986; Zang, Krist, Erlebader, & Hussaini, 1987). They can provide better resolution but lack physically realistic representation (Joslin et al. 1992).

Second, although there have been some spatial studies (Fasel, 1976; Fasel & Bestek, 1986; Fasel & Konzelmann, 1990; Spalart, 1989; Danabasoglu, Biringen, & Streett, 1991), the spatial direct numerical simulation (DNS) is still in its early age (Kleiser & Zang, 1991). Most of these can predict only the early stages of transition (pre-onset simulation) or fully developed turbulent flow without a transition process and require high CPU cost which is in the range of 100-1000 CRAY-YMP CPU hours.

In contrast, the current study has two advantages. First, it was successful in spatial DNS for the whole process of transition including linear evolution, secondary instability, breakdown, and transition to turbulence. Second, the current approach is more efficient. The spatial DNS was carried out on a rather coarse grid ($16 \times 34 \times 34$ for each T-S wavelength) at an acceptable CPU cost which is in the range of 2 - 10 CRAY-YMP hours.

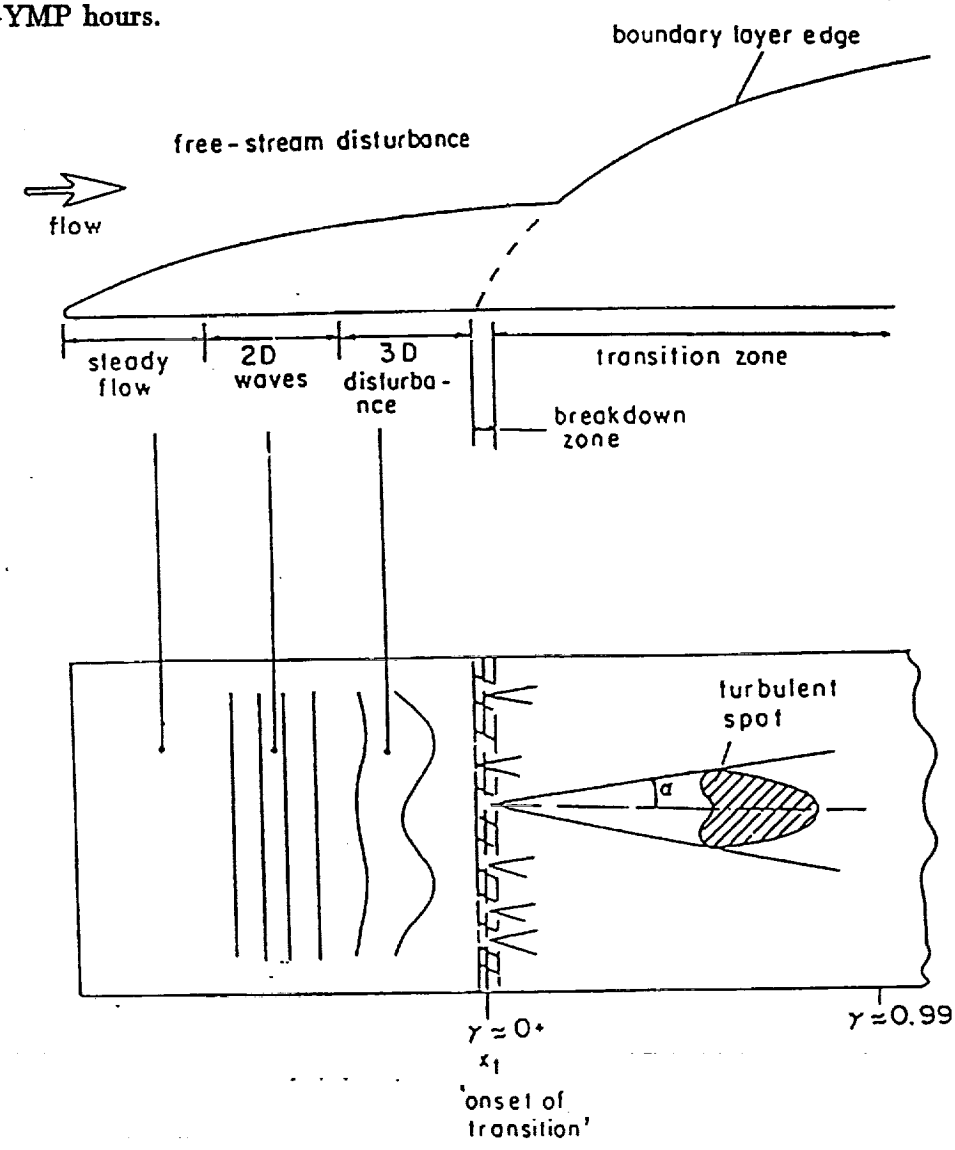

Figure 1. Idealized sketch of transition process on a flat plate.

2 Governing Equation In General Coordinates

Let

$$\begin{aligned} x &= x(\xi,\eta,\zeta), \\ y &= y(\xi,\eta,\zeta), \\ z &= z(\xi,\eta,\zeta), \end{aligned}$$

the 3-D time-dependent incompressible Navier-Stokes equations can then be written as

$$U = \frac{1}{J}(u\xi_x + v\xi_y + w\xi_z), \tag{1}$$

$$V = \frac{1}{J}(u\eta_x + v\eta_y + w\eta_z), \tag{2}$$

$$W = \frac{1}{J}(u\zeta_x + v\zeta_y + w\zeta_z), \tag{3}$$

and

$$\frac{\partial u}{\partial t} + J(\frac{\partial Uu}{\partial \xi} + \frac{\partial Vu}{\partial \eta} + \frac{\partial Wu}{\partial \zeta}) + (\xi_x\frac{\partial}{\partial \xi} + \eta_x\frac{\partial}{\partial \eta} + \zeta_x\frac{\partial}{\partial \zeta})P - \frac{1}{Re}\Delta_1 u = 0, \tag{4}$$

$$\frac{\partial v}{\partial t} + J(\frac{\partial Uv}{\partial \xi} + \frac{\partial Vv}{\partial \eta} + \frac{\partial Wv}{\partial \zeta}) + (\xi_y\frac{\partial}{\partial \xi} + \eta_y\frac{\partial}{\partial \eta} + \zeta_y\frac{\partial}{\partial \zeta})P - \frac{1}{Re}\Delta_1 v = 0, \tag{5}$$

$$\frac{\partial w}{\partial t} + J(\frac{\partial Uw}{\partial \xi} + \frac{\partial Vw}{\partial \eta} + \frac{\partial Ww}{\partial \zeta}) + (\xi_z\frac{\partial}{\partial \xi} + \eta_z\frac{\partial}{\partial \eta} + \zeta_z\frac{\partial}{\partial \zeta})P - \frac{1}{Re}\Delta_1 w = 0, \tag{6}$$

$$\frac{\partial U}{\partial \xi} + \frac{\partial V}{\partial \eta} + \frac{\partial W}{\partial \zeta} = 0, \tag{7}$$

where u, v, w are velocity components, U, V, W are contravariant velocity components, P is pressure, Re is the Reynolds number based on the free stream velocity U_∞, the viscosity parameter ν and some reference length, for example, δ_0^* which is the displacement thickness of boundary layer at inflow,

$$Re = \frac{U_\infty \delta_0^*}{\nu},$$

and Δ_1 is the physical Laplacian operator transferred to the computational (ξ,η,ζ) space:

$$\begin{aligned} \Delta_1 &= (\xi_x^2+\xi_y^2+\xi_z^2)\frac{\partial^2}{\partial \xi^2} + (\eta_x^2+\eta_y^2+\eta_z^2)\frac{\partial^2}{\partial \eta^2} + (\zeta_x^2+\zeta_y^2+\zeta_z^2)\frac{\partial^2}{\partial \zeta^2} + 2(\xi_x\eta_x+\xi_y\eta_y+\xi_z\eta_z)\frac{\partial^2}{\partial \xi \partial \eta} \\ &+ 2(\xi_x\zeta_x+\xi_y\zeta_y+\xi_z\zeta_z)\frac{\partial^2}{\partial \xi \partial \zeta} + 2(\eta_x\zeta_x+\eta_y\zeta_y+\eta_z\zeta_z)\frac{\partial^2}{\partial \eta \partial \zeta} + (\xi_{xx}+\xi_{yy}+\xi_{zz})\frac{\partial}{\partial \xi} \\ &+ (\eta_{xx}+\eta_{yy}+\eta_{zz})\frac{\partial}{\partial \eta} + (\zeta_{xx}+\zeta_{yy}+\zeta_{zz})\frac{\partial}{\partial \zeta}. \end{aligned} \tag{8}$$

Here, we have 7 equations for 7 unknowns, u, v, w, P, U, V, and W.

The perturbation equations are obtained by decomposing the total flow into steady base flow and a perturbation. Using subscript 0 denote the base flow variables, and let

$$\begin{aligned} \vec{v}(x,y,z,t) &\leftarrow \vec{v}_0(x,y,z) \pm \vec{v}(x,y,z,t), \\ \vec{V}(x,y,z,t) &\leftarrow \vec{V}_0(x,y,z) + \vec{V}(x,y,z,t), \\ P(x,y,z,t) &\leftarrow P_0(x,y,z) + P(x,y,z,t), \end{aligned} \tag{9}$$

where $\vec{v} = (u, v, w)$, $\vec{V} = (U, V, W)$, and noting the base flow itself also satisfies the Navier-Stokes equations, we obtain the governing system for the perturbations:

$$\begin{aligned}
&\frac{\partial u}{\partial t} + J(\frac{\partial[u(U+U_0)+u_0U]}{\partial \xi} + \frac{\partial[u(V+V_0)+u_0V]}{\partial \eta} + \\
&\frac{\partial[u(W+W_0)+u_0W]}{\partial \zeta}) + (\xi_x\frac{\partial}{\partial \xi} + \eta_x\frac{\partial}{\partial \eta} + \zeta_x\frac{\partial}{\partial \zeta})P - \frac{1}{Re}\Delta_1 u &= 0, \qquad (10)\\
&\frac{\partial v}{\partial t} + J(\frac{\partial[v(U+U_0)+v_0U]}{\partial \xi} + \frac{\partial[v(V+V_0)+v_0V]}{\partial \eta} + \\
&\frac{\partial[v(W+W_0)+v_0W]}{\partial \zeta}) + (\xi_y\frac{\partial}{\partial \xi} + \eta_y\frac{\partial}{\partial \eta} + \zeta_y\frac{\partial}{\partial \zeta})P - \frac{1}{Re}\Delta_1 v &= 0, \qquad (11)\\
&\frac{\partial w}{\partial t} + J(\frac{\partial[w(U+U_0)+w_0U]}{\partial \xi} + \frac{\partial[w(V+V_0)+w_0V]}{\partial \eta} + \\
&\frac{\partial[w(W+W_0)+w_0W]}{\partial \zeta}) + (\xi_z\frac{\partial}{\partial \xi} + \eta_z\frac{\partial}{\partial \eta} + \zeta_z\frac{\partial}{\partial \zeta})P - \frac{1}{Re}\Delta_1 w &= 0, \qquad (12)\\
&\frac{\partial U}{\partial \xi} + \frac{\partial V}{\partial \eta} + \frac{\partial W}{\partial \zeta} &= 0, \qquad (13)
\end{aligned}$$

Combined with (1)-(3), this system also has 7 equations and 7 unknowns for the perturbations.

We perform the solving process as follows:

1. Perform the surface and grid generation processes to obtain the required Jacobian coefficients.
2. Solve system (1) – (7) to obtain the base flow solution. For a flat plate, we use the Blasius similarity solution for the base flow.
3. Solve system (1) – (3) and (10) – (13) to obtain the perturbation solution based on the above base flow.

3 Boundary Conditions

Benney-Lin type disturbances are imposed at the inflow boundary in this study:

$$\begin{aligned}
u(0,y,z,t) &= \epsilon_{2d} Real\{\phi_{u2d} e^{-i\omega t}\} \\
&+ \epsilon_{3d+} Real\{\phi_{u3d+} e^{i(\beta z - \omega t)}\} \\
&+ \epsilon_{3d-} Real\{\phi_{u3d-} e^{i(-\beta z - \omega t)}\}, \\
v(-\frac{\Delta x}{2},y,z,t) &= \epsilon_{2d} Real\{\phi_{v2d} e^{i(-\alpha\frac{\Delta x}{2} - \omega t)}\} \\
&+ \epsilon_{3d+} Real\{\phi_{v3d+} e^{i(-\alpha\frac{\Delta x}{2} + \beta z - \omega t)}\} \\
&+ \epsilon_{3d-} Real\{\phi_{v3d-} e^{i(-\alpha\frac{\Delta x}{2} - \beta z - \omega t)}\}, \\
w(-\frac{\Delta x}{2},y,z,t) &= \epsilon_{3d+} Real\{\phi_{w3d+} e^{i(-\alpha\frac{\Delta x}{2} + \beta z - \omega t)}\} \\
&+ \epsilon_{3d-} Real\{\phi_{w3d-} e^{i(-\alpha\frac{\Delta x}{2} - \beta z - \omega t)}\},
\end{aligned} \qquad (14)$$

where ω is the real frequency of the disturbance, β is a real constant that represents the spanwise wavenumber, and $\alpha = \alpha_R + i\alpha_I$ is the streamwise complex wavenumber obtained from linear stability theory. ϕ_u, ϕ_v and ϕ_w are eigenfunctions for the Orr-Sommerfeld equation.

A no slip boundary condition is applied at the solid wall. According to the linear stability theory, the disturbances vanish at infinity, so we obtain the boundary conditions at far field given by

$$\begin{aligned} u(x, y \to \infty, z, t) &= 0, \\ v(x, y \to \infty, z, t) &= 0, \\ w(x, y \to \infty, z, t) &= 0. \end{aligned} \tag{15}$$

Also, no pressure condition is needed at the inflow, solid wall, or far field since a staggered grid is used.

4 Outflow Boundary Treatment

Outflow boundary conditions have been the focus of study for the spatial simulation of flow transition by many researchers. For simplicity, we only describe the idea for a 2-D flat plate. The technique for the 3-D problem is the same.

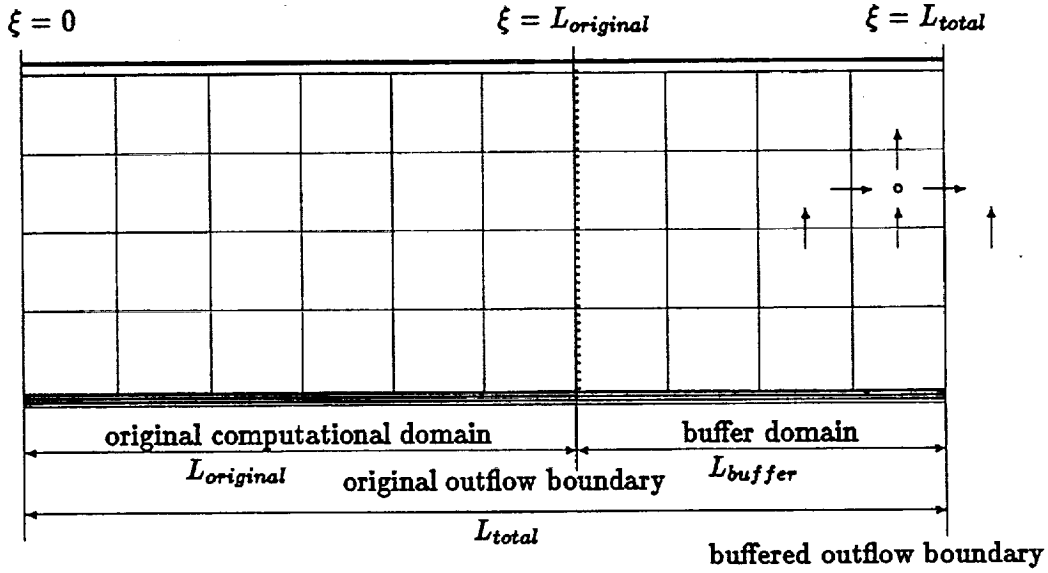

Figure 2. Extended computational domain.

Taking the advantage of the staggered grid, we can obtain a fairly effective approach. First, a buffer domain technique developed by Streett & Macaraeg (1989) is applied to our problem. Thus, a buffer domain is appended to the end of the original outflow boundary to smear all possible reflections from the buffered outflow boundary (see Figure 2). The problem is, in general, that the conventional buffer domain is too long (usually four to eight T-S wavelengths), which greatly increases computation cost. Our goal is to maintain the accuracy in the original computational domain, and to eliminate all the possible reflection waves in a very short buffer domain. To realize the above goal, the governing equations in the buffer domain should be parabolicized to allow only strictly outgoing waves. Thus, a first buffer function $b(\xi)$ is introduced here and applied to the streamwise viscous terms:

$$\frac{\partial^2 U}{\partial \xi^2} \to b(\xi)\frac{\partial^2 U}{\partial \xi^2}, \qquad \frac{\partial^2 V}{\partial \xi^2} \to b(\xi)\frac{\partial^2 V}{\partial \xi^2}. \tag{16}$$

$b(\xi)$ is a monotonically decreasing function that changes from 1 to 0 so that the upstream effects of the streamwise viscous terms will gradually disappear in the buffer domain. The essential feature here is that all damping mode disturbances at the buffered outflow boundary become zero. To understand this, we rewrite the first equation of (16) as

$$b(\xi)\frac{\partial^2 U}{\partial \xi^2} \to \frac{\partial^2 U}{\partial [\frac{\xi}{\sqrt{b(\xi)}}]^2}. \tag{17}$$

Since $b(\xi) \to 0$ at the buffered outflow boundary, and accordingly $\frac{\xi}{\sqrt{b(\xi)}} \to \infty$, then, we can also consider that the buffered outflow boundary is compressed from $\xi = \infty$ by the function $\sqrt{b(\xi)}$. Now clearly, if the disturbances are stable (damping modes), they will vanish at $\xi = \infty$. To treat unstable (growing) modes, we need a second buffer function $b_{Re}(\xi)$ that reduces the Reynolds number in the buffer domain gradually to less than the critical (or subcritical) Reynolds number and makes all the perturbation modes become damping

$$\frac{1}{Re} \to \frac{b_{Re}(\xi)}{Re}. \tag{18}$$

Thus, the new modified governing equations in the computational (ξ, η) plane become:

$$\begin{aligned}
&\frac{\partial U}{\partial t} + \frac{1}{y_\eta}\frac{\partial (UU + 2U_0U)}{\partial \xi} + \frac{\partial}{\partial \eta}\left(\frac{U_0V + UV_0 + UV}{y_\eta}\right) \\
&-\frac{b_{Re}}{Re_0^*}\left(b \cdot \frac{\partial^2 U}{\partial \xi^2} + \frac{1}{y_\eta}\frac{\partial^2}{\partial \eta^2}\left(\frac{U}{y_\eta}\right) + y_\eta \eta_{yy}\frac{\partial}{\partial \eta}\left(\frac{U}{y_\eta}\right)\right) + y_\eta \frac{\partial P}{\partial \xi} &= 0, \qquad (19)\\
&y_\eta \frac{\partial V}{\partial t} + \frac{\partial (U_0V + UV_0 + UV)}{\partial \xi} + \frac{\partial (2V_0V + VV)}{\partial \eta} \\
&-\frac{b_{Re}}{Re_0^*}\left(b \cdot y_\eta \frac{\partial^2 V}{\partial \xi^2} + \frac{1}{y_\eta}\frac{\partial^2 V}{\partial \eta^2} + y_\eta \eta_{yy}\frac{\partial V}{\partial \eta}\right) + \frac{\partial P}{\partial \eta} &= 0, \qquad (20)\\
&\frac{\partial U}{\partial \xi} + \frac{\partial V}{\partial \eta} &= 0. \qquad (21)
\end{aligned}$$

The buffer functions are chosen as follows:

$$\begin{aligned}
b(\xi) &= \begin{cases} \frac{tanh(L_{total} - \xi)}{tanh(L_{buffer})} & L_{original} \le \xi \le L_{total}\,, \\ 1 & 0 \le \xi \le L_{original}\,, \end{cases} \\
b_{Re}(\xi) &= \begin{cases} c\frac{(\xi - L_{original})^2}{L_{buffer}^2} + 1 & L_{original} \le \xi \le L_{total}, \\ 1 & 0 \le \xi \le L_{original}. \end{cases}
\end{aligned} \tag{22}$$

It is clear that the first function decreases from one to zero very rapidly as one moves from the original outflow boundary to the buffered outflow boundary. The second function increasing from 1 to $c + 1$ is a quadratic function that is continuously differentiable at the original outflow boundary. Note that the total effect of these buffer functions is that, toward the buffered outflow boundary:

- the momentum equations become increasingly convection dominated in the $\xi-$direction, while the equations generally become parabolic; and
- the momentum equations become highly diffusion dominated in the $\eta-$direction.

This treatment makes the outgoing waves propagate forward without reflection in the $\xi-$direction, and any oscillation in the $\eta-$direction will be effectively smeared in the buffer domain.

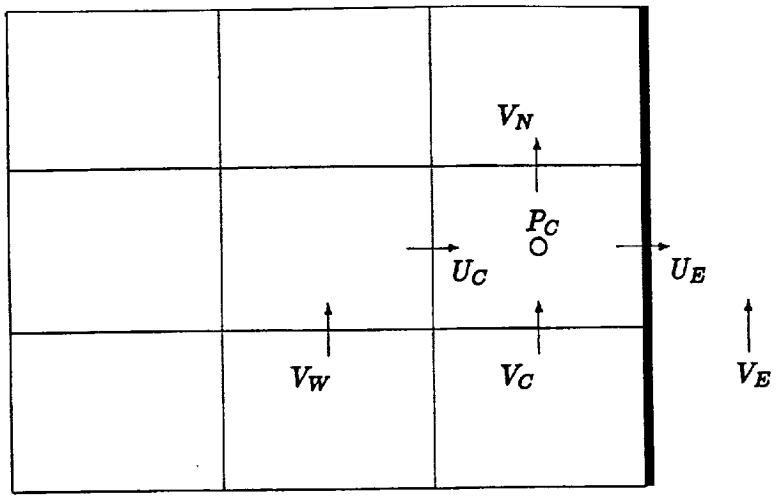

Figure 3. Buffered outflow boundary points.

Finally, we need to specify the buffered outflow boundary conditions under these modified governing equations. The parabolic character of the above equations requires only two boundary conditions. As mentioned before, we have the disturbances tending to zero at the buffered outflow boundary (which is actually located at $\xi = \infty$), so one condition is

$$P = 0. \tag{23}$$

This is a very important condition since the elliptic character of pressure has not been modified in our new governing equation. Any improper condition for P may cause trouble. For the second condition, we use the traditional extrapolation method for V, i.e.,

$$\frac{\partial^2 V}{\partial \xi^2} = 0. \tag{24}$$

Though this condition may not be so accurate, accuracy of solutions in the buffer domain is not so important, and the main concern is that there must be no reflection wave traveling back to the original computational domain.

Referring to Figure 3, condition (23) is imposed directly on P by defining

$$P_C = 0. \tag{25}$$

This is an implicit condition. With it, the discrete continuity equation associated with P_C is then used to define U at the buffered boundary:

$$U_E = U_C - \frac{V_N - V_C}{\Delta \eta} \Delta \xi. \tag{26}$$

Condition (24) is imposed by determining V at ghost points just outside the boundary:

$$V_E = 2V_C - V_W. \tag{27}$$

Note that the above treatment is only suitable for the perturbation equations.

5 Simplification

In this study, we still use rectangular but stretched grids obtained by a special but relatively simple mapping (Figure 4):

$$\begin{aligned} x &= \xi, \\ y &= y(\eta), \\ z &= \zeta. \end{aligned} \tag{28}$$

This yields

$$\begin{aligned} J &= \eta_y, \\ \xi_x &= \zeta_z = 1, \\ \xi_y &= \zeta_z = \eta_x = \eta_z = \zeta_x = \zeta_y = 0. \end{aligned} \tag{29}$$

For our numerical simulation, we choose the transformation function

$$y(\eta) = \frac{y_{max}\sigma\eta}{\eta_{max}\sigma + y_{max}(\eta_{max} - \eta)}, \tag{30}$$

where y_{max} is the height of the computational domain in the physical coordinates y, η_{max} is the height of the computational domain in the computational coordinate η, and σ is a constant which can be used to adjust the concentration of grid points. This yields an inverse map

$$\eta(y) = \frac{\eta_{max}y(\sigma + y_{max})}{y_{max}(\sigma + y)}. \tag{31}$$

We can then obtain

$$y_\eta = \frac{\eta_{max}y_{max}\sigma(\sigma + y_{max})}{[\eta_{max}\sigma + y_{max}(\eta_{max} - \eta)]^2}, \tag{32}$$

$$\eta_{yy} = -\frac{2\eta_{max}\sigma(\sigma + y_{max})}{y_{max}(\sigma + y)^3}. \tag{33}$$

Figure 4. y-direction stretched grid.

Under the above mapping, the governing equations can be simplified:

$$\frac{\partial u}{\partial t} + \eta_y\left(\frac{\partial[u(U+U_0)+u_0U]}{\partial\xi} + \frac{\partial[u(V+V_0)+u_0V]}{\partial\eta} + \frac{\partial[uW+u_0W]}{\partial\zeta}\right) + \frac{\partial P}{\partial\xi} - \frac{1}{Re}\Delta_1 u = 0, \tag{34}$$

$$\frac{\partial v}{\partial t} + \eta_y\left(\frac{\partial[v(U+U_0)+v_0U]}{\partial\xi} + \frac{\partial[v(V+V_0)+v_0V]}{\partial\eta} + \frac{\partial[vW+v_0W]}{\partial\zeta}\right) + \eta_y\frac{\partial P}{\partial\eta} - \frac{1}{Re}\Delta_1 v = 0, \tag{35}$$

$$\frac{\partial w}{\partial t} + \eta_y\left(\frac{\partial[w(U+U_0)+w_0U]}{\partial \xi} + \frac{\partial[w(V+V_0)+w_0V]}{\partial \eta} + \frac{\partial[wW+w_0W]}{\partial \zeta}\right) + \frac{\partial P}{\partial \zeta} - \frac{1}{Re}\Delta_1 w = 0, \quad (36)$$

$$\frac{\partial U}{\partial \xi} + \frac{\partial V}{\partial \eta} + \frac{\partial W}{\partial \zeta} = 0, \quad (37)$$

$$U = \frac{u}{\eta_y}, \quad (38)$$

$$W = \frac{w}{\eta_y}, \quad (39)$$

$$V = v, \quad (40)$$

where u, v, w, P, U, V, W are all fluctuating parts of the corresponding variables, and $u_0, v_0, w_0, U_0, V_0, W_0$ represent the base flow (Blasius solution for the flat plate). The transferred Laplacian operator in the computational space is simplified as

$$\Delta_1 = \frac{\partial^2}{\partial \xi^2} + \eta_y^2\frac{\partial^2}{\partial \eta^2} + \frac{\partial^2}{\partial \zeta^2} + \eta_{yy}\frac{\partial}{\partial \eta} \quad (41)$$

6 Discretization

We use a uniform staggered grid for our problem in the computational (ξ, η, ζ) space (Figure 5). Letting ϕ denote a generic function, the second-order backward Euler difference in time direction can be written as

$$\frac{\partial \phi}{\partial t} \sim \frac{3\phi^{n+1} - 4\phi^n + \phi^{n-1}}{2\Delta t}, \quad (42)$$

and the fourth-order central difference in space can be written as

$$\frac{\partial \phi}{\partial \xi}(\xi) \sim \frac{-\phi(\xi+2\Delta\xi) + 8\phi(\xi+\Delta\xi) - 8\phi(\xi-\Delta\xi) + \phi(\xi-2\Delta\xi)}{12\Delta\xi}, \quad (43)$$

$$\frac{\partial \phi^2}{\partial \xi^2}(\xi) \sim \frac{-\phi(\xi+2\Delta\xi) + 16\phi(\xi+2\Delta\xi) - 30\phi(\xi) + 16\phi(\xi-\Delta\xi) - \phi(\xi-2\Delta\xi)}{12\Delta\xi^2}, \quad (44)$$

$$\frac{\partial \phi}{\partial \xi}(\xi + \frac{1}{2}\Delta\xi) \sim \frac{-\phi(\xi+2\Delta\xi) + 27\phi(\xi+\Delta\xi) - 27\phi(\xi) + \phi(\xi-\Delta\xi)}{24\Delta\xi}. \quad (45)$$

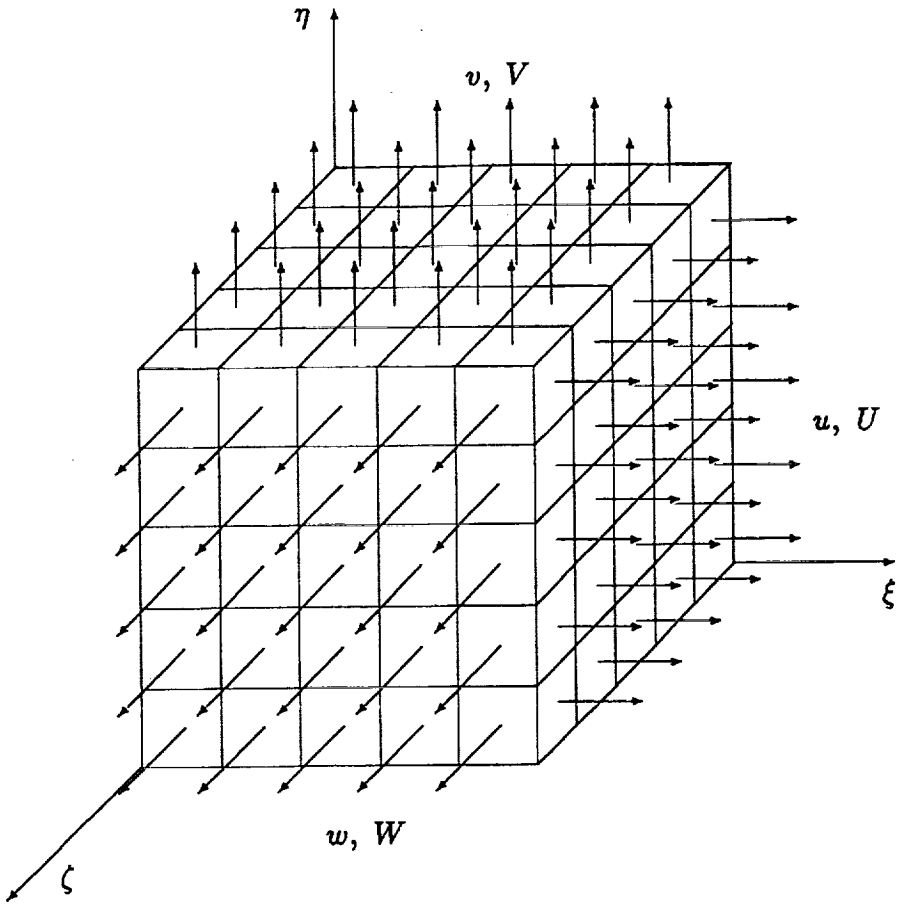

Figure 5. Staggered grid structure in the computational (ξ, η, ζ) space.

In the computational $(\xi,\ \eta,\ \zeta)$ space, the grids are uniform. Suppose u, v, w and U, V, W are defined in terms of a staggered grid in the computational space (see Figure 5). Here, the values of P are associated with its cell centers, u and U with centers of the cell surfaces parallel to the (η, ζ) plane, v and V with centers of the cell surfaces parallel to the (ξ, ζ) plane, and w and W with centers of the cell surfaces parallel to the (ξ, η) plane.

Second-order backward Euler differences are used in the time direction, and fourth-order central differences are used in space. We can write the discretized governing equations symbolically as follows (Figure 6):

$$\begin{aligned}
A_{EE}u_{EE} + A_E u_E + A_W u_W + A_{WW}u_{WW} + A_{NN}u_{NN} + A_N u_N \ &+ \\
A_S u_S + A_{SS}u_{SS} + A_{FF}u_{FF} + A_F u_F + A_B u_B + A_{BB}u_{BB} \ &- \\
A_C u_C + D_{WW}P_{WW} + D_W P_W + D_E P_E - D_C P_C \ &= \ S_u, \qquad (46) \\
B_{EE}v_{EE} + B_E v_E + B_W v_W + B_{WW}v_{WW} + B_{NN}v_{NN} + B_N v_N \ &+ \\
B_S v_S + B_{SS}v_{SS} + B_{FF}v_{FF} + B_F v_F + B_B v_B + B_{BB}v_{BB} \ &- \\
B_C v_C + E_{SS}P_{SS} + E_S P_S + E_N P_N - E_C P_C \ &= \ S_v, \qquad (47) \\
C_{EE}w_{EE} + C_E w_E + C_W w_W + C_{WW}w_{WW} + C_{NN}w_{NN} + C_N w_N \ &+ \\
C_S w_S + C_{SS}w_{SS} + C_{FF}w_{FF} + C_F w_F + C_B w_B + C_{BB}w_{BB} \ &- \\
C_C w_C + F_{BB}P_{BB} + F_B P_B + F_F P_F - F_C P_C \ &= \ S_w, \qquad (48) \\
DU_{EE}U_{EE} + DU_E U_E + DU_W U_W - DU_C U_C + DV_{NN}V_{NN} \ &+ \\
+DV_N V_N + DV_S V_S - DV_C V_C + DW_{FF}W_{FF} \ &+ \\
DW_F W_F + DW_B W_B - DW_C W_C \ &= \ S_M. \qquad (49)
\end{aligned}$$

As an illustration of the notation we use, relevant symbols for the discrete ξ-momentum equation are depicted in Figure 4. The coefficients and source term for the interior points of the discrete $\xi-$momentum equation (46)

associated with u_C are given as follows:

$$
\begin{aligned}
A_{EE} &= -\frac{1}{12Re\Delta\xi^2} + \frac{\eta_{yC}}{12\Delta\xi}(U_{EE} + 2U_{0_{EE}}),\\
A_E &= \frac{4}{3Re\Delta\xi^2} - \frac{2\eta_{yC}}{3\Delta\xi}(U_E + 2U_{0_E}),\\
A_W &= \frac{4}{3Re\Delta\xi^2} + \frac{2\eta_{yC}}{3\Delta\xi}(U_W + 2U_{0_W}),\\
A_{WW} &= -\frac{1}{12Re\Delta\xi^2} - \frac{2\eta_{yC}}{12\Delta\xi}(U_{WW} + 2U_{0_{WW}}),\\
A_{NN} &= -\frac{\alpha_C}{12Re\Delta\eta^2} + \frac{\eta_{yC}}{12\Delta\eta}(V_{nn} + V_{0nn}) - \frac{\gamma_C}{12Re\Delta\eta},\\
A_N &= \frac{4\alpha_C}{3Re\Delta\eta^2} - \frac{2\eta_{yC}}{3\Delta\eta}(V_n + V_{0n}) + \frac{2\gamma_C}{3Re\Delta\eta},\\
A_S &= \frac{4\alpha_C}{3Re\Delta\eta^2} + \frac{2\eta_{yC}}{3\Delta\eta}(V_s + V_{0s}) - \frac{2\gamma_C}{3Re\Delta\eta},\\
A_{SS} &= -\frac{\alpha_C}{12Re\Delta\eta^2} - \frac{\eta_{yC}}{12\Delta\eta}(V_{ss} + V_{0ss}) + \frac{\gamma_C}{12Re\Delta\eta},\\
A_{FF} &= -\frac{1}{12Re\Delta\zeta^2} + \frac{\eta_{yC}}{12\Delta\zeta}(W_{ff} + W_{0_{ff}}),\\
A_F &= \frac{4}{3Re\Delta\zeta^2} - \frac{2\eta_{yC}}{3\Delta\zeta}(W_f + W_{0_f}),\\
A_B &= \frac{4}{3Re\Delta\zeta^2} + \frac{2\eta_{yC}}{3\Delta\zeta}(W_b + W_{0_b}),\\
A_{BB} &= -\frac{1}{12Re\Delta\zeta^2} - \frac{\eta_{yC}}{12\Delta\zeta}(W_{bb} + W_{0_{bb}}),\\
A_C &= \frac{3}{2\Delta t} + \frac{5}{2Re}\left(\frac{1}{\Delta\xi^2} + \frac{\alpha_C}{\Delta\eta^2} + \frac{1}{\Delta\zeta^2}\right),\\
D_E &= \frac{1}{24\Delta\xi},\\
D_W &= D_C = \frac{27}{24\Delta\xi},\\
D_{WW} &= -\frac{1}{24\Delta\xi},\\
S_u &= \frac{-4u_C^n + u_C^{n-1}}{2\Delta t} + \eta_{yC}\left(\frac{-u_{0NN}V_{nn} + 8u_{0N}V_n - 8u_{0S}V_s + u_{0SS}V_{ss}}{12\Delta\eta}\right.\\
&\quad \left. + \frac{-u_{0FF}W_{ff} + 8u_{0F}W_f - 8u_{0B}W_b + u_{0BB}W_{bb}}{12\Delta\zeta}\right).
\end{aligned}
\tag{50}
$$

Here, superscripts n and $n-1$ are used to indicate values at previous time steps, and superscript $n+1$, which indicates the current time step, is dropped for convenience. Lower case subscripts denote the approximate values of the v and w at points where the associated values of u with capital subscript are located (Figure 6). Other symbols used in the above formulas are as follows:

$$
\alpha = \eta_y^2, \qquad \gamma = \eta_{yy}. \tag{51}
$$

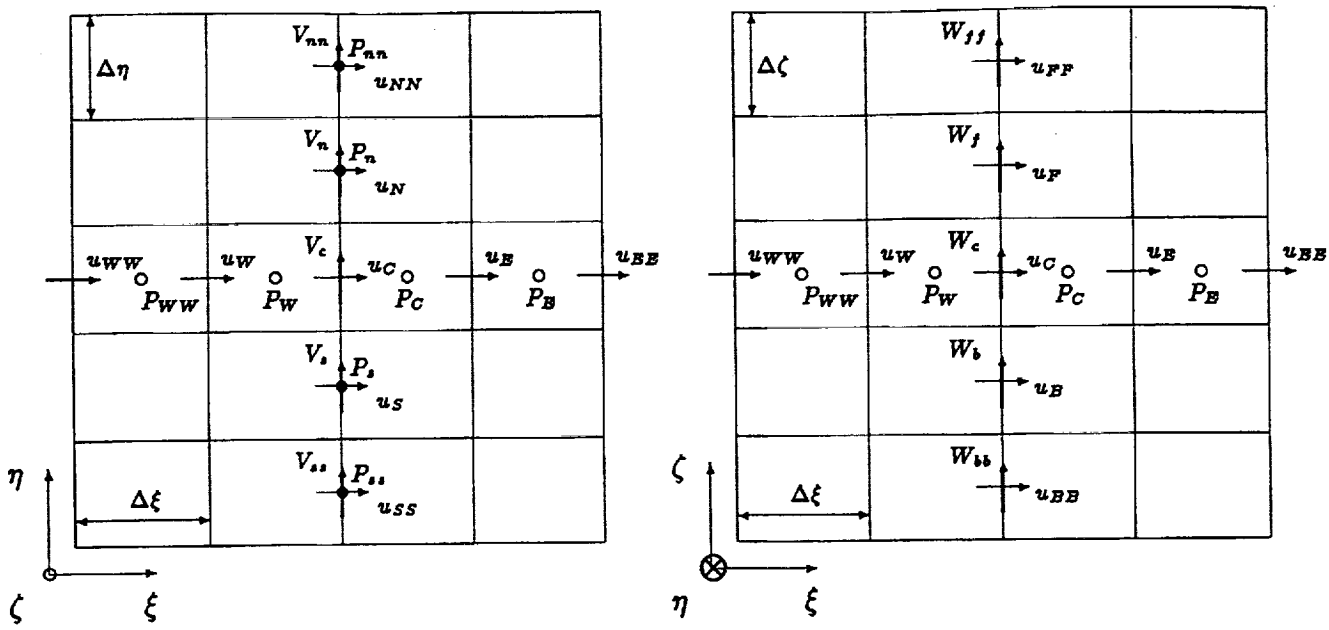

Figure 6. Neighbor points for ξ-momentum equation
(U are at the same points as u and are not shown here).

All function values that are required at other than the canonical locations are obtained by fourth-order interpolations in the computational space. For example (see Figure 7),

$$V_c = (9(V_C + V_N + V_{NW} + V_W) - (V_{SWW} + V_{NNWW} + V_{SE} + V_{NNE}))/32, \quad (52)$$

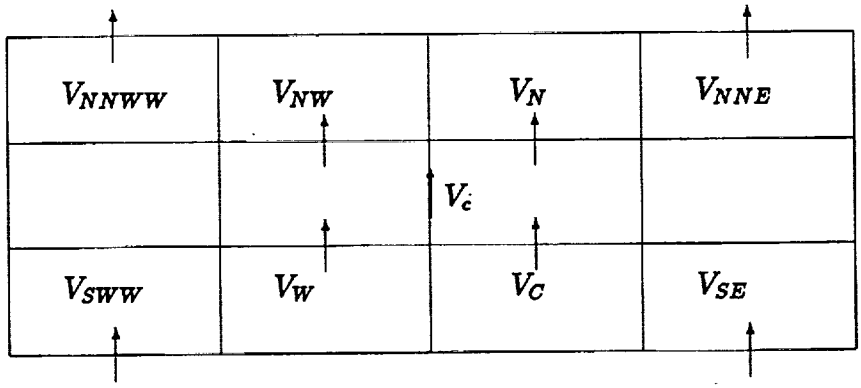

Figure 7. Neighbor points for fourth-order approximation for V_c.

The coefficients for the $\eta-$ and $\zeta-$ momentum equations are defined in an analogous way, and the discrete continuity equation is developed simply by applying the fourth-order central differences to each term.

7 Approximate Line-Box Relaxation (ALB)

7.1 2-D uniform grids

The basic approximate box relaxation (AB) approach is to relax by boxes instead of points. With a 2-D uniform grid (Figure 8) as an example, we first describe the basic idea behind AB.

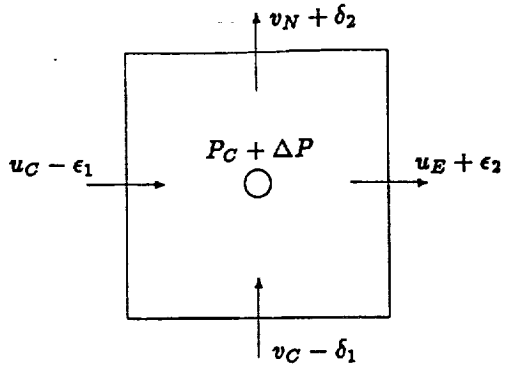

Figure 8. Approximate box relaxation.

The generic form of the equations associated with a box for the 2-D uniform grids can be written as

$$A_E^C u_E + A_W^C u_W + A_N^C u_N + A_S^C u_S - A_C^C u_C + \frac{P_W - P_C}{\Delta x} = S_{u_C}, \tag{53}$$

$$A_E^E u_{EE} + A_W^E u_C + A_N^E u_{NE} + A_S^E u_{SE} - A_C^E u_E + \frac{P_C - P_E}{\Delta x} = S_{u_E}, \tag{54}$$

$$B_E^C v_E + B_W^C v_W + B_N^C v_N + B_S^C v_S - B_C^C v_C + \frac{P_S - P_C}{\Delta y} = S_{v_C}, \tag{55}$$

$$B_E^N v_{NE} + B_W^N v_{NW} + B_N^N v_{NN} + B_S^N v_C - B_C^N v_N + \frac{P_C - P_N}{\Delta y} = S_{v_N}, \tag{56}$$

$$\frac{u_E - u_C}{\Delta x} + \frac{v_N - v_C}{\Delta y} = 0. \tag{57}$$

Here, the superscripts represent the point at which the discretization is centered. We proceed in the box-by-box process with a few global point Gauss-Seidel relaxation sweeps on the momentum equations, changing u and v and holding P fixed. This means that the four momentum equations (53)-(56) in the box phase are approximately satisfied. Now, proceeding by boxes in some order, we perform distributed relaxation of the form:

$$\begin{aligned} u_C &\leftarrow u_C - \epsilon_1, \\ u_E &\leftarrow u_E + \epsilon_2, \\ v_C &\leftarrow v_C - \delta_1, \\ v_N &\leftarrow v_N + \delta_2, \\ P_C &\leftarrow P_C + \Delta P, \end{aligned} \tag{58}$$

where the corrections are chosen to satisfy the discrete continuity equation and four discrete momentum equations associated with the box. Note that the old values of u, v, and P approximately satisfy the associated momentum equations, so we obtain the following system for the corrections, ϵ_1, ϵ_2, δ_1, δ_2, and ΔP:

$$\begin{aligned} (A_E^C \epsilon_2 + A_C^C \epsilon_1) - \frac{\Delta P}{\Delta x} &= 0, \\ (A_C^E \epsilon_2 + A_W^E \epsilon_1) - \frac{\Delta P}{\Delta x} &= 0, \\ (B_N^C \delta_2 + B_C^C \delta_1) - \frac{\Delta P}{\Delta y} &= 0, \\ (B_C^N \delta_2 + B_S^N \delta_1) - \frac{\Delta P}{\Delta y} &= 0, \\ \frac{\epsilon_1 + \epsilon_2}{\Delta x} + \frac{\delta_1 + \delta_2}{\Delta y} &= S_m, \end{aligned} \tag{59}$$

where

$$S_m = -\left(\frac{u_E - u_C}{\Delta x} + \frac{v_N - v_C}{\Delta y}\right).$$

(59a) and (59b) yield

$$\frac{\epsilon_1}{\epsilon_2} = \alpha \equiv \frac{A_C^E - A_E^C}{A_C^C - A_W^E},$$

(59c) and (59d) yield

$$\frac{\delta_1}{\delta_2} = \beta \equiv \frac{B_C^N - B_N^C}{B_C^C - B_S^N},$$

and together we have

$$\frac{\epsilon_1}{\delta_1} = \gamma \equiv \frac{B_C^C + \frac{B_N^C}{\beta}}{A_C^C + \frac{A_E^C}{\alpha}} \cdot \frac{\Delta y}{\Delta x}.$$

Therefore, (59e) can be written as

$$\frac{\epsilon_1 + \frac{\epsilon_1}{\alpha}}{\Delta x} + \frac{\delta_1 + \frac{\delta_1}{\beta}}{\Delta y} = S_m, \tag{60}$$

or

$$\frac{\gamma(1 + \frac{1}{\alpha})\delta_1}{\Delta x} + \frac{(1 + \frac{1}{\beta})\delta_1}{\Delta y} = S_m. \tag{61}$$

The correction are thus given by

$$\begin{aligned} \delta_1 &= \frac{S_m}{\frac{\gamma(1+\frac{1}{\alpha})}{\Delta x} + \frac{(1+\frac{1}{\beta})}{\Delta y}}, \\ \delta_2 &= \frac{\delta_1}{\beta}, \\ \epsilon_1 &= \delta_1 \cdot \gamma, \\ \epsilon_2 &= \frac{\epsilon_1}{\alpha}, \end{aligned} \tag{62}$$

and

$$\Delta P = (A_C^C \epsilon_1 + A_E^C \epsilon_2) \cdot \Delta x.$$

To simplify this scheme, note that for the case $\Delta t << 1$, we have

$$\begin{aligned} A_C^C \sim A_C^E, \quad & B_C^C \sim B_C^N, \\ A_C^E >> A_E^C, \quad & A_C^C >> A_W^E, \\ B_C^N >> B_N^C, \quad & B_C^C >> B_S^N, \end{aligned}$$

so

$$\begin{aligned} \alpha &\approx 1, \\ \beta &\approx 1, \\ \gamma &\approx \frac{\Delta y}{\Delta x}. \end{aligned}$$

For most cases, we have

$$\begin{aligned} A_C^E > A_E^C, \quad & A_C^C > A_W^E, \\ B_C^N > B_N^C, \quad & B_C^C > B_S^N, \end{aligned}$$

so α, β and γ can be approximated in general by

$$\begin{aligned} \alpha &\sim \frac{A_C^E}{A_C^C} \sim 1, \\ \beta &\sim \frac{B_C^N}{B_C^C} \sim 1, \\ \gamma &\sim \frac{B_C^C}{A_C^C} \cdot \frac{\Delta y}{\Delta x}. \end{aligned}$$

It is these approximations and update formulas in (62) that we use in AB.

7.2 General coordinates

For general coordinates, the discrete momentum equations can still be written in the same generic form as that for Cartesian coordinates, but the continuity equation is changed to

$$\frac{U_E - U_C}{\Delta\xi} + \frac{V_N - V_C}{\Delta\eta} = 0. \tag{63}$$

The physical velocities u and v have the following relations with the contravariant velocities U and V:

$$\begin{aligned} U &= au + bv, \\ V &= cu + dv. \end{aligned}$$

This leads to the discrete continuity equation written as

$$\frac{a_E u_E + b_E \tilde{v}_E - a_C u_C - b_C \tilde{v}_C}{\Delta\xi} + \frac{c_N \tilde{u}_N + d_N v_N - c_C \tilde{u}_C - d_C v_C}{\Delta\eta} = 0,$$

where the superscript $\sim$ represents a point that is not located at a canonical position and therefore requires interpolation. Assuming that

$$(b_E \Delta\tilde{v}_E - b_C \Delta\tilde{v}_C) < (a_E \Delta u_E - a_C \Delta u_C), \tag{64}$$

$$(c_N \Delta\tilde{u}_N - c_C \Delta\tilde{u}_C) < (d_N \Delta v_N - d_C \Delta v_C), \tag{65}$$

then the correspond correction equation can be approximated by

$$\frac{a_E \epsilon_2 + a_C \epsilon_1}{\Delta\xi} + \frac{d_N \delta_2 + d_C \delta_1}{\Delta\eta} = S_m.$$

Note that the defining relations for $\epsilon_1, \epsilon_2, \delta_1$, and δ_2 can be expressed in the same form as for Cartesian coordinates:

$$\begin{aligned} \frac{\epsilon_1}{\epsilon_2} &= \alpha, \\ \frac{\delta_1}{\delta_2} &= \beta, \\ \frac{\epsilon_1}{\delta_1} &= \gamma, \end{aligned}$$

and

$$\delta_1 = \frac{S_m}{\frac{(\frac{a_E}{\alpha} + a_C)\gamma}{\Delta\xi} + \frac{(\frac{d_N}{\beta} + d_C)}{\Delta\eta}}, \tag{66}$$

where a_E, a_C, d_N, d_C correspond to the mapping coefficients between u, v and U, V.

7.3 Approximate line-box relaxation (ALB) for 3-D problems

AB usually works well for 2-D problems, but frequently fails to provide fast convergence for 3-D problems. The basic idea of ALB is to satisfy the continuity equation for all boxes lying on one line simultaneously. Figure 9 gives the distribution of corrections in the (ξ, η) plane for the ALB. This kind of relaxation is very useful when the grids are anisotropic. Assuming for simplicity that $\alpha = \beta = 1$, then according to Figure 9, ALB solving the discrete system (46)–(49) can be described as follows:

- Freezing P, U, V, W, v, and w, perform line Gauss-Seidel relaxation on (46) over the entire computational domain to obtain a new u.
- Freezing P, U, V, W, u, and w, perform line Gauss-Seidel relaxation on (47) over the entire computational domain to obtain a new v.
- Freezing P, U, V, W, u, and v, perform line Gauss-Seidel relaxation on (48) over the entire computational domain to obtain a new w.
- Use transformation (38)–(40) to obtain new U, V, W.

- For all $j = 2, 3, \cdots, n_j - 1$ at once: change $U_{i-\frac{1}{2}\ jk}, U_{i+\frac{1}{2}\ jk}, V_{ij-\frac{1}{2}\ k}, W_{ijk-\frac{1}{2}}$, and $W_{ijk+\frac{1}{2}}$ to satisfy the associated continuity equations, then update P_{ijk} so that the new U, V, W and P as well as the associated transferred u, v, w satisfy the three momentum equations.

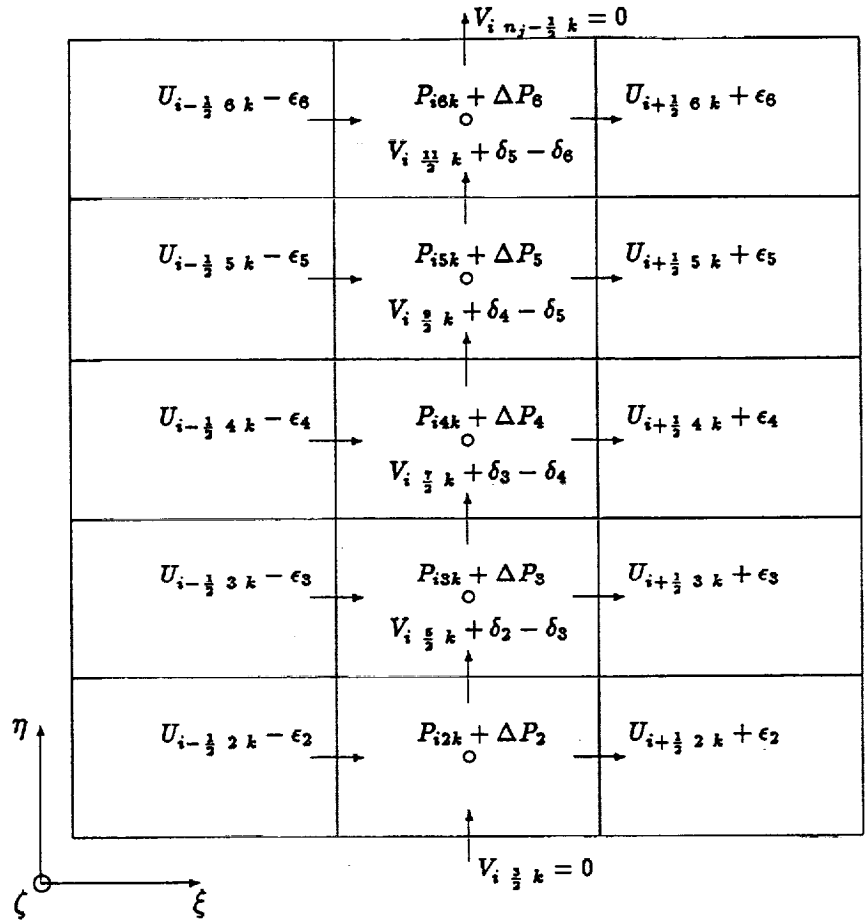

Figure 9. Distribution of corrections in the (ξ, η) plane.

Since all of the u, v, w have been previously relaxed, and the U, V, W are updated, we assume that equations (46)–(48) hold exactly. Let ϵ, δ, σ and ΔP represent the corrections for U, V, W and P, respectively. Thus, for cube ijk (see Figure 9), the correction equations corresponding to (46)–(49) are

$$(A^{i-\frac{1}{2}\ jk}_{i+\frac{1}{2}\ jk}\eta_{y_{i+\frac{1}{2}\ jk}} + A^{i-\frac{1}{2}\ jk}_{i-\frac{1}{2}\ jk}\eta_{y_{i-\frac{1}{2}\ jk}})\epsilon_j - D^{i-\frac{1}{2}\ jk}_{ijk}\Delta P_j = 0, \tag{67}$$

$$B^{ij-\frac{1}{2}\ k}_{ij+\frac{1}{2}\ k}(\delta_j - \delta_{j+1}) - B^{ij-\frac{1}{2}\ k}_{ij-\frac{1}{2}\ k}(\delta_{j-1} - \delta_j) - E^{ij-\frac{1}{2}\ k}_{ijk}\Delta P_j = 0, \tag{68}$$

$$(C^{ijk-\frac{1}{2}}_{ijk+\frac{1}{2}}\eta_{y_{ijk+\frac{1}{2}}} + C^{ijk-\frac{1}{2}}_{ijk-\frac{1}{2}}\eta_{y_{ijk-\frac{1}{2}}})\sigma_j - F^{ijk-\frac{1}{2}}_{ijk}\Delta P_j = 0, \tag{69}$$

$$\begin{aligned}(DU^{ijk}_{i+\frac{1}{2}\ jk} + DU^{ijk}_{i-\frac{1}{2}\ jk})\epsilon_j + (DW^{ijk}_{ijk+\frac{1}{2}} + DW^{ijk}_{ijk-\frac{1}{2}})\sigma_j \\ + DV^{ijk}_{ij+\frac{1}{2}\ k}(\delta_j - \delta_{j+1}) - DV^{ijk}_{ij-\frac{1}{2}\ k}(\delta_{j-1} - \delta_j) = S_{m_{ijk}}, \\ j = 2, 3, \cdots, n_j - 1,\end{aligned} \tag{70}$$

where the superscripts represent the point at which the discretization is centered. This system has $4(n_j - 2)$ equations for $4(n_j - 2)$ variables. Unfortunately, coupling between the correction variables makes the problem somewhat complicated. To develop a simpler approximate system, define

$$\omega_{xj} = \frac{\epsilon_j}{\delta_j},$$

$$\omega_{xj} = \frac{\sigma_j}{\delta_j}.$$

Then, equation (70) can be written in terms of the unknowns δ_j only:

$$[(DU^{ijk}_{i+\frac{1}{2}\ jk} + DU^{ijk}_{i-\frac{1}{2}\ jk})\omega_{xj} + (DV^{ijk}_{ij+\frac{1}{2}\ k} + DV^{ijk}_{ij-\frac{1}{2}\ k}) + (DW^{ijk}_{ijk+\frac{1}{2}} + DW^{ijk}_{ijk-\frac{1}{2}})\omega_{zj}]\delta_j$$
$$-DV^{ijk}_{ij-\frac{1}{2}\ k}\delta_{j-1} - DV^{ijk}_{ij+\frac{1}{2}\ k}\delta_{j+1} = S_{m_{ijk}}. \tag{71}$$

Let

$$\begin{aligned} a_j &= (DU^{ijk}_{i+\frac{1}{2}\ jk} + DU^{ijk}_{i-\frac{1}{2}\ jk})\omega_{xj} + (DV^{ijk}_{ij+\frac{1}{2}\ k} + DV^{ijk}_{ij-\frac{1}{2}\ k}) \\ &\quad +(DW^{ijk}_{ijk+\frac{1}{2}} + DW^{ijk}_{ijk-\frac{1}{2}})\omega_{zj}, && (72)\\ b_j &= -DV^{ijk}_{ij+\frac{1}{2}\ k}, && (73)\\ c_j &= -DV^{ijk}_{ij-\frac{1}{2}\ k}, && (74)\\ & \qquad j = 2, 3, \cdots, n_j - 1. \end{aligned}$$

Then we obtain the tridiagonal system

$$\begin{bmatrix} a_2 & b_2 & & & & \\ c_3 & a_3 & b_3 & & & \\ & \ddots & \ddots & \ddots & & \\ & & \ddots & \ddots & \ddots & \\ & & & c_{n_j-2} & a_{n_j-2} & b_{n_j-2} \\ & & & & c_{n_j-1} & a_{n_j-1} \end{bmatrix} \begin{bmatrix} \delta_2 \\ \delta_3 \\ \vdots \\ \vdots \\ \delta_{n_j-2} \\ \delta_{n_j-1} \end{bmatrix} = \begin{bmatrix} S_{m\ i\ 2\ k} \\ S_{m\ i\ 2\ k} \\ \vdots \\ \vdots \\ S_{m\ i\ n_j-2\ k} \\ S_{m\ i\ n_j-1\ k} \end{bmatrix}. \tag{75}$$

Thus, $\delta_j,\ j = 2, 3, \cdots, n_j - 1$ can be determined very efficiently. The other velocity corrections are given by

$$\begin{aligned} \epsilon_j &= \omega_{xj}\delta_j, \\ \sigma_j &= \omega_{zj}\delta_j, \\ & \qquad j = 2, 3, \cdots, n_j - 1. \end{aligned}$$

The U, V, and W are then updated on all cells in the i, k η–line as follows:

$$\begin{aligned} U_{i+\frac{1}{2}\ jk} &\leftarrow U_{i+\frac{1}{2}\ jk} + \epsilon_j, \\ U_{i-\frac{1}{2}\ jk} &\leftarrow U_{i-\frac{1}{2}\ jk} - \epsilon_j, \\ W_{ij\ k+\frac{1}{2}} &\leftarrow W_{ij\ k+\frac{1}{2}} + \sigma_j, \\ W_{ijk-\frac{1}{2}} &\leftarrow W_{ijk-\frac{1}{2}} - \sigma_j, && (76)\\ & \qquad j = 2, 3, \cdots, n_j - 1, \\ V_{ij-\frac{1}{2}k} &\leftarrow V_{ij-\frac{1}{2}k} + \delta_{j-1} - \delta_j, && (77)\\ & \qquad j = 3, 4, \cdots, n_j - 1. \end{aligned}$$

P is then updated via

$$\begin{aligned} P_{ijk} &\leftarrow P_{ijk} + \Delta P_j, && (78)\\ & j = 2, 3, \cdots, n_j - 1. \end{aligned}$$

8 Semi-Coarsening Multigrid

For the large-scale algebraic system of the 3-D flows that must be solved at each time step, the usual relaxation methods by themselves are much too slow. To obtain optimal efficiency, we use a multigrid scheme based on AB and ALB described in the previous section. For simplicity of discussion, we consider only the two-grid case.

We use a full approximation scheme(FAS) to accommodate nonlinearities. A two-level FAS algorithm for an equation of the form

$$L^h\phi^h = f^h \tag{79}$$

may be described loosely as follows:

i) relax on $L^h\phi^h = f^h$,

ii) solve $L^{2h}\phi^{2h} = L^{2h}I_h^{2h}\phi^h + \tilde{I}_h^{2h}(f^h - L^h\phi^h)$,

iii) replace $\phi^h \leftarrow \phi^h + I_{2h}^h(\phi^{2h} - I_h^{2h}\phi^h)$.

The notation we have introduced includes the difference operators L^h and L^{2h}, the restriction operators I_h^{2h} (for the approximation) and $\tilde{I}_h^{2h}$ (for the residual), and the interpolation operator I_h^{2h}.

A full-coarsening strategy is generally ineffective for problems that favor special coordinate directions (e.g., anisotropic problems). To overcome this limitation, we consider now a special combination of semi-coarsening and line-box relaxation. The basic idea is to use line-box relaxation in one direction (say the y-direction) and coarsening only in the other two directions (x- and z-directions). A two-level staggered grid projected in the (x, y)-plane and (x, z)-plane is given in Figure 10.

The full weighting restriction is still used here for transferring the residual from fine to coarse grids. The stencils can be expressed as follows:

$$\begin{aligned}
\tilde{I}_h^{2h}(R_u) &: \begin{bmatrix} \frac{1}{8} & \frac{1}{4} & \frac{1}{8} \\ \frac{1}{8} & \frac{1}{4} & \frac{1}{8} \end{bmatrix}, \\
\tilde{I}_h^{2h}(R_v) &: \begin{bmatrix} \frac{1}{4} & \frac{1}{4} \\ \frac{1}{4} & \frac{1}{4} \end{bmatrix}, \\
\tilde{I}_h^{2h}(R_w) &: \begin{bmatrix} \frac{1}{8} & \frac{1}{8} \\ \frac{1}{4} & \frac{1}{4} \\ \frac{1}{8} & \frac{1}{8} \end{bmatrix}, \\
\tilde{I}_h^{2h}(R_m) &: \begin{bmatrix} \frac{1}{4} & \frac{1}{4} \\ \frac{1}{4} & \frac{1}{4} \end{bmatrix}.
\end{aligned} \tag{80}$$

These stencils can be explained geometrically as shown in Figures 11-12.

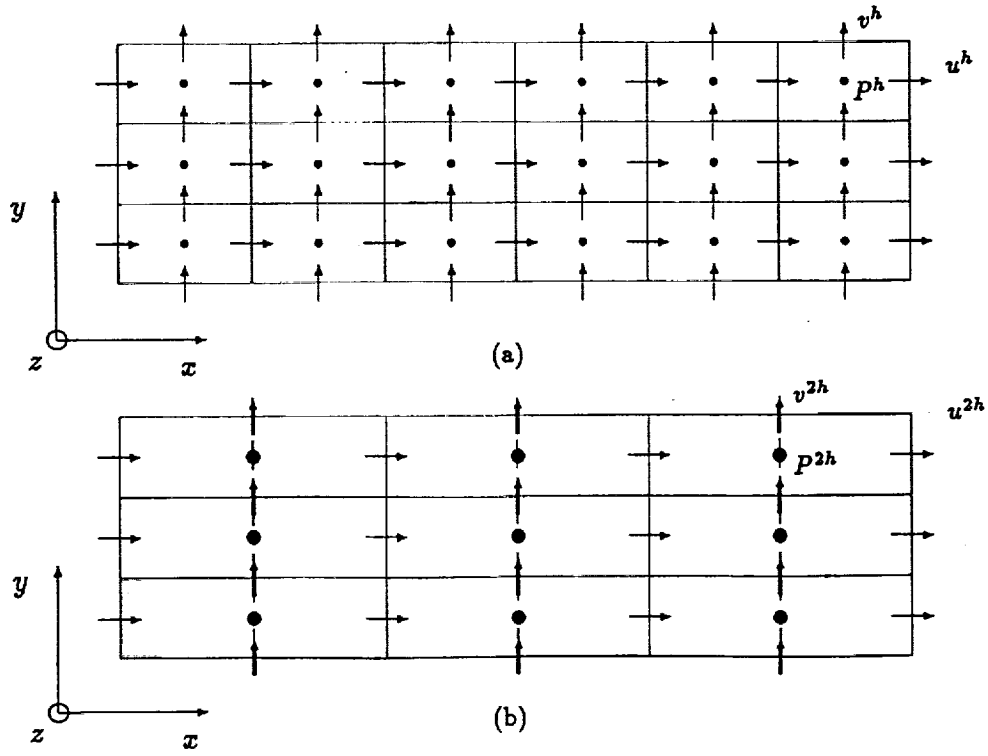

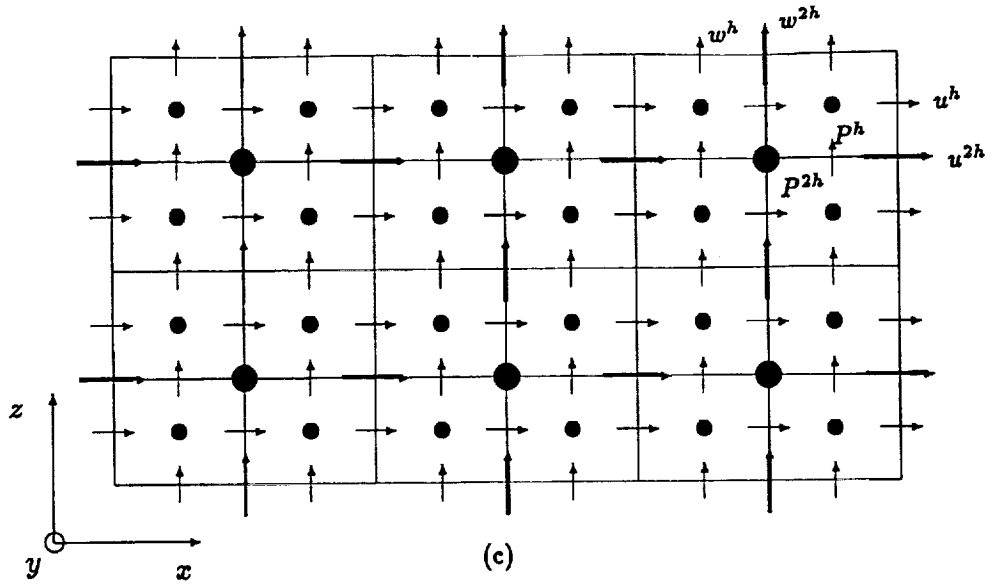

Figure 10. Two-level staggered grid structure for $x-z$ direction semi-coarsening: (a) fine grid projection on (x,y) plane, (b) coarse grid projection on (x,y) plane, (c) fine and coarse grid projection on (x,z) plane.

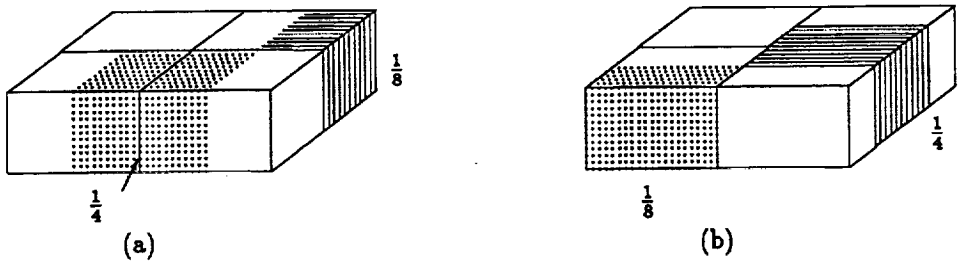

Figure 11. Full-weighting restriction for (a) x-momentum equation, (b) z-momentum equation.

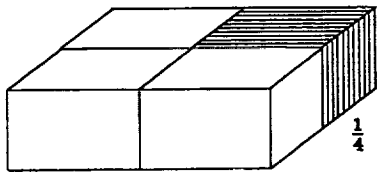

Figure 12. Full-weighting restriction for y-momentum and continuity equations.

For the restriction of variables, bilinear interpolation is used. Its stencils are

$$\begin{aligned}
\bar{I}_h^{2h}(u) &: \begin{bmatrix} \frac{1}{2} \\ \frac{1}{2} \end{bmatrix}, \\
\bar{I}_h^{2h}(v) &: \begin{bmatrix} \frac{1}{4} & \frac{1}{4} \\ \frac{1}{4} & \frac{1}{4} \end{bmatrix}, \\
\bar{I}_h^{2h}(w) &: \begin{bmatrix} \frac{1}{2} & \frac{1}{2} \end{bmatrix}, \\
\bar{I}_h^{2h}(P) &: \begin{bmatrix} \frac{1}{4} & \frac{1}{4} \\ \frac{1}{4} & \frac{1}{4} \end{bmatrix}.
\end{aligned} \tag{81}$$

For semi-coarsening, the coarse to fine transfer operators are based on linear interpolation:

$$\bar{I}_{2h}^{h}(\Delta u) \;:\; \begin{bmatrix} \frac{3}{4} \\ \frac{1}{4} \end{bmatrix} \quad \text{for} \quad \Delta u_1^h \quad \text{or} \quad \begin{bmatrix} \frac{3}{8} & \frac{3}{8} \\ \frac{1}{8} & \frac{1}{8} \end{bmatrix} \quad \text{for} \quad \Delta u_2^h,$$

$$
\begin{aligned}
\tilde{I}^h_{2h}(\Delta v) \quad &: \quad \begin{bmatrix} \frac{3}{16} & \frac{9}{16} \\ \frac{1}{16} & \frac{3}{16} \end{bmatrix}, \\
\tilde{I}^h_{2h}(\Delta w) \quad &: \quad \begin{bmatrix} \frac{3}{4} & \frac{1}{4} \end{bmatrix} \quad \text{for} \quad \Delta w^h_1 \quad \text{or} \quad \begin{bmatrix} \frac{3}{8} & \frac{1}{8} \\ \frac{3}{8} & \frac{1}{8} \end{bmatrix} \quad \text{for} \quad \Delta w^h_2, \\
\tilde{I}^h_{2h}(\Delta P) \quad &: \quad \begin{bmatrix} \frac{3}{16} & \frac{9}{16} \\ \frac{1}{16} & \frac{3}{16} \end{bmatrix}.
\end{aligned} \tag{82}
$$

The meaning of the above stencils is shown in Figures 13-15.

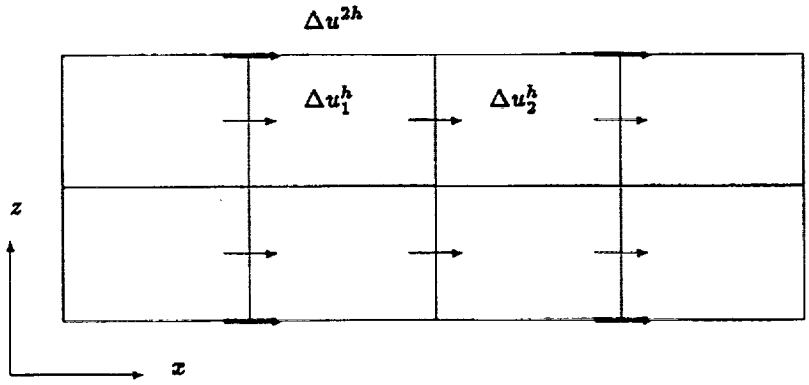

Figure 13. Bilinear interpolation for Δu.

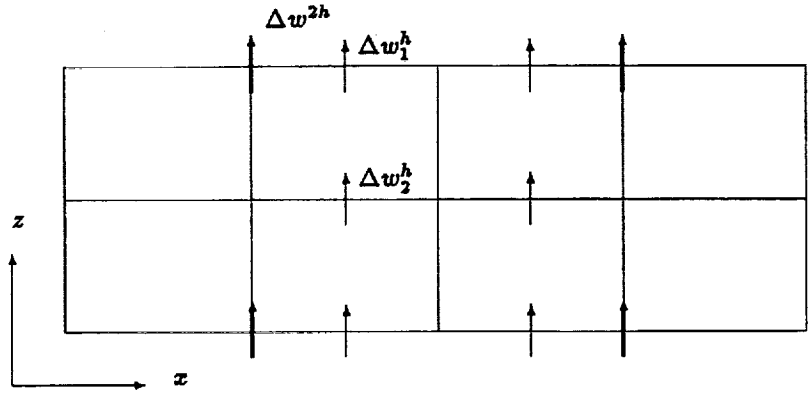

Figure 14. Bilinear interpolation for Δw.

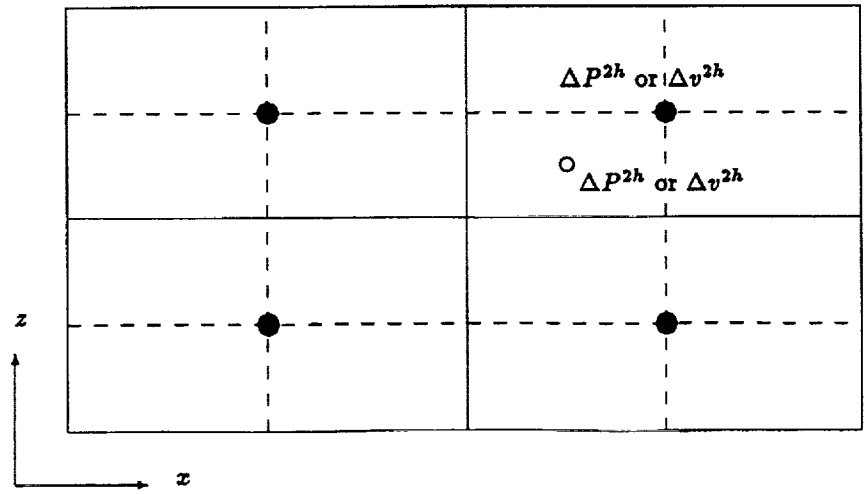

Figure 15. Bilinear interpolation for Δv and ΔP,
(ΔP and Δv are not located in the same (x, z) plane).

9 Fine-Coarse-Fine Grid Mapping

The spatial DNS usually meets difficulties after the flow goes into the breakdown stage when the shear layer is developed and the vortex breaks down to small scale vortices. The numerical simulation will thus have a huge energy burst, and the disturbance velocity will be amplified by tens or hundreds of times somewhere inside the flow field . The code then blows up. Apparently, it is not the physical case, but is largely caused by that the grid we used is not fine enough to resolve the small eddies which play the role to generate dissipations. To keep the numerical simulation going, we developed a fine-coarse-fine grid mapping technique. To explain this technique, let us see what happens for a 1-D problem. We do the fine to coarse grid restriction and the coarse to fine grid interpolation at each time step:

$$\begin{aligned} u_c &= I_h^{2h} u_f^{old} \\ u_f^{new} &= I_{2h}^h u_c \end{aligned}$$

Here, I_h^{2h} is a linear restriction and I_{2h}^h is a linear interpolation.

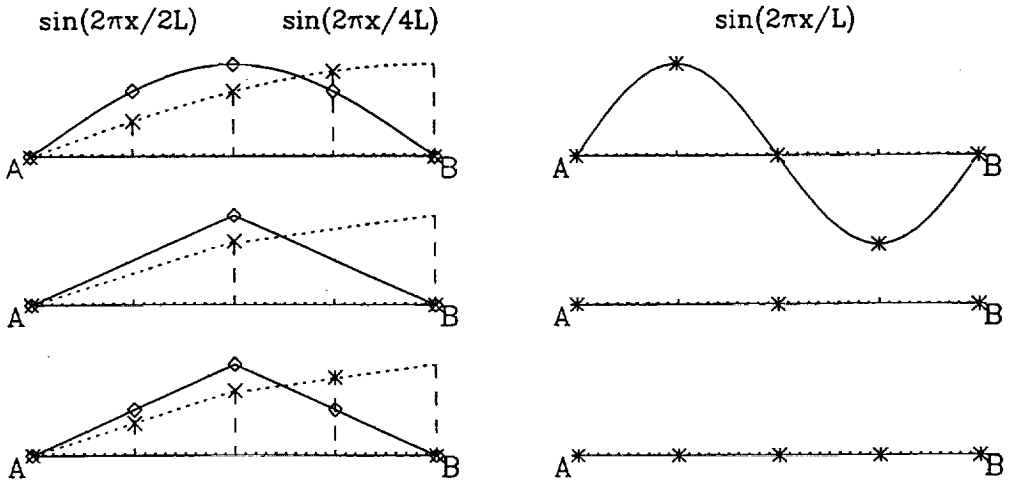

$K < 1$ modes $K = 1$ modes

Figure 16. Fine-coarse-fine mapping.

Define L as a section which has five grid points on the fine grid, and (assume $u_A \equiv 0$)

$$\alpha = \frac{\int_0^L |u_f^{new}| dx}{\int_0^L |u_f^{old}| dx}$$

as the amplification factor.

Assume we have different frequency modes, e.g.,

$$\sin(K\frac{2\pi}{L}x), \quad K = 1, \frac{1}{2}, \frac{1}{4}, \frac{1}{8}, \cdots$$

($K > 1$ is not visible on this grid), we can approximately get α by numerical integration for different modes.

$$\begin{aligned} \alpha &= \frac{[\sin(K\frac{2\pi}{L}\frac{L}{2}) + \frac{1}{2}\sin(K\frac{2\pi}{L}L)]\frac{L}{2}}{[\sin(K\frac{2\pi}{L}\frac{L}{4}) + \sin(K\frac{2\pi}{L}\frac{L}{2})\sin(K\frac{2\pi}{L}\frac{3L}{4}) + \frac{1}{2}\sin(K\frac{2\pi}{L}L)]\frac{L}{4}} \\ &= \frac{2\sin(K\pi) + \sin(2K\pi)}{\sin(\frac{K\pi}{2}) + \sin(K\pi) + \sin(\frac{3}{2}K\pi) + \frac{1}{2}\sin(2K\pi)}, \end{aligned}$$

when $K = 1$, $\alpha = 0$, when $K \to 0$, $\alpha \to 1$.

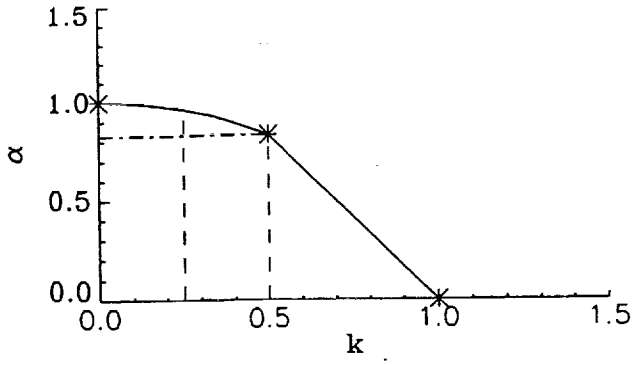

Figure 17. Amplification factor for different modes.

Figure 17 clearly shows that this kind of grid mapping, fine to coarse restriction and coarse to fine interpolation, significantly damps the highest frequency ($K = 1$), but has only a little effect on other modes ($K < 1$), and has almost no effect on low frequency modes ($K \to 0$).

The computational resources are still quite limited for DNS even if we use today's largest supercomputer. For certain grids, the highest frequency which can be well simulated is $K = 1$. This highest mode may generate higher frequencies which can not be simulated by current grids and may cause the computation to fail. This fine-coarse-fine grid mapping damps the $K = 1$ mode and protects other frequency modes. Of course, we do not want to eliminate the $K = 1$ mode, but to restrict its energy growth. The actual procedure of this technique is

1. $u_c = I_h^{2h} u_f^{old}$,
2. $u_f^{new} = (1 - \beta) u_f^{old} + \beta I_{2h}^h u_c$.

Here, we choose

$$\beta = \gamma \cdot (u^2 + v^2 + w^2),$$

which is proportional to the perturbation energy. Therefore, there is very little damping to $K = 1$ when the perturbation is very small. In this way, we successfully keep the code running to simulate the whole process of transition: linear evolution, secondary instability, breakdown, and transition. Note that the large eddies play a much more important role in flow transition than do small eddies which correspond to high frequency modes. We have to sacrifice these small eddies due to the lack of computer resources. But, the physics of transition and turbulence are still simulated quite well due to the accurate representation of lower frequency modes corresponding to large eddies.

10 Computational Results

10.1 Comparison with linear stability theory (LST)

To verify the accuracy of our approach, we compare our results with the linear theory by assuming a parallel steady base flow and imposing a small disturbance at inflow. The base flow is now $u_0(x, y) = u_0(x_0, y)$, $v_0(x, y) = 0$, where $u_0(x_0, y)$ is the Blasius similarity solution at inflow. Since it is easy for finite difference schemes to simulate the damping (stable) modes, we just test the growing (unstable) modes.

Let $Re_0^* = 900$, $Fr = 86$ ($\omega = 0.0774$), and $\beta = 0$ (2-D case). The Orr-Sommerfeld solution provides an eigenvalue

$$\alpha = \alpha_R + i\alpha_I = 0.2229 - i0.00451,$$

and the associated eigenfunctions $\phi_R^u, \phi_I^u, \phi_R^v$, and ϕ_I^v which are dependent only on y (Figure 18).

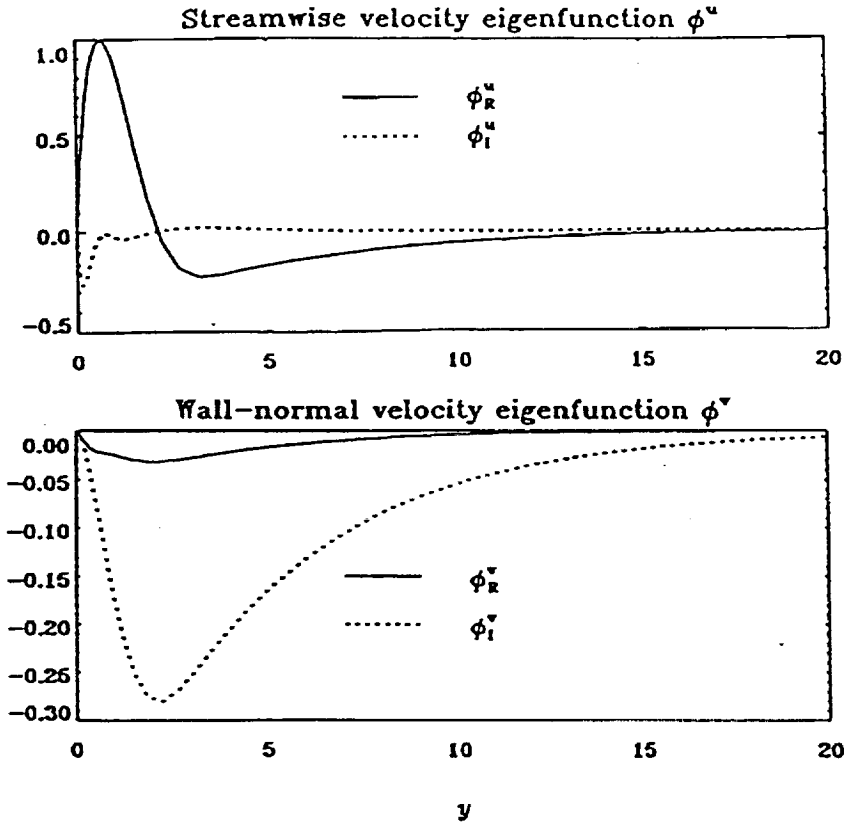

Figure 18. Streamwise and wall-normal velocity eigenfunctions of an unstable mode ($Re_0^* = 900$) in 2-D flat plate flow.

In LST, the disturbances are assumed to be traveling waves. In the 2-D case, this yields

$$u = \epsilon e^{-\alpha_I x}(\phi_R^u cos(\alpha_R x - \omega_R t) - \phi_I^u sin(\alpha_R x - \omega_R t)),$$
$$v = \epsilon e^{-\alpha_I x}(\phi_R^v cos(\alpha_R x - \omega_R t) - \phi_I^v sin(\alpha_R x - \omega_R t)). \quad (83)$$

The inflow boundary velocities can then be obtained by setting $x = x_0$ for u and $x = x_0 - \frac{\Delta x}{2}$ for v (x_0 is the $x-$coordinate at inflow). We assume that ϵ is small. Figure 18 shows the complex eigenfunctions for both u and v components ($\phi_R^u, \phi_I^u, \phi_R^v$, and ϕ_I^v) in the physical $(x, y)-$ plane, which are normalized by setting $max\{\phi_R^u\} \equiv 1$.

A moderate computational domain is selected. In this case, the plate length (measured from the inflow location $x = x_0$) is set to eleven Tollmien-Schlichting (T-S) wavelengths, while the buffer domain is an additional single wavelength, making the length of the total computational domain twelve T-S wavelengths. Here we choose $y_{max} = 75$ and use a total computational grid with 362×50 grid points. The grid is highly anisotropic near the solid wall ($\Delta x \gg \Delta y$).

Since we use a fully-implicit scheme, the time step is restricted mainly by accuracy consideration. For our tests, we take

$$\Delta t = \frac{2\pi}{320\omega} = 0.2537.$$

The convergence rate of the semi-coarsening multigrid method, which we generally found to be about 0.2 per V(2,2) cycle (relax twice on each grid level before descending and ascending), is much better than the performance of single-grid relaxation, as shown in Figure 19.

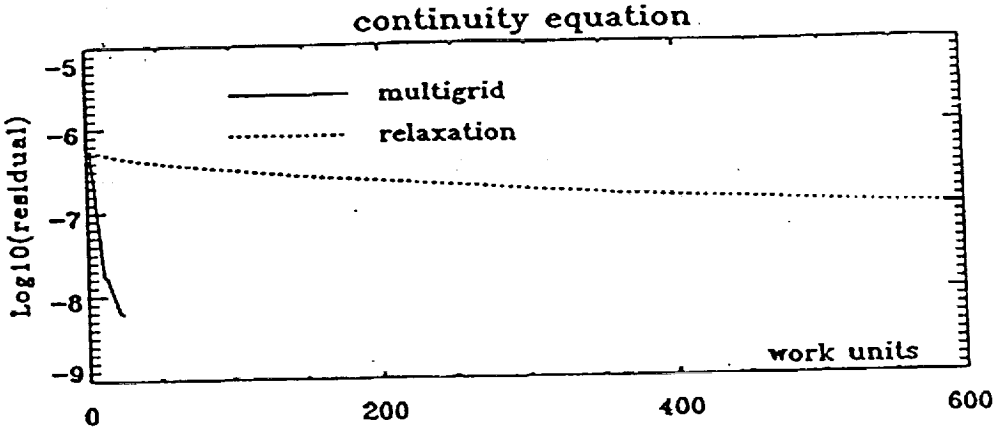

Figure 19. Convergence history at a fixed time for multigrid and single-grid relaxation.

In order to compare the computational results with the linear theory solution, which is accurate for the parallel wall-bounded base flow with small disturbances, we first assume that the base flow is everywhere given by

$$U_0(\xi,\eta) = U_0(0,\eta), \quad V_0(\xi,\eta) = 0, \quad \text{and} \quad \epsilon = 10^{-4},$$

where, $U_0(0,\eta)$ is the Blasius similarity solution in the computational (ξ,η) plane at $\xi = 0$ and that the displacement thickness of the boundary layer is a constant, $\delta^*_{x_0}$. Then $Re^*(= Re^*_0), \alpha$, and ω do not change along the streamwise direction. The streamwise and wall-normal velocity components, u and v, of the disturbance after 13 T-S periods (t=13T) are compared with the solutions obtained by the linear theory at a vertical position close to the solid wall ($y^* = 1.3137$ for u and $y^* = 1.2448$ for v) in Figure 20. Excellent agreement in both amplitude and phase between the computational results of our fourth-order finite difference scheme and the solution obtained by LST is observed in the physical domain.

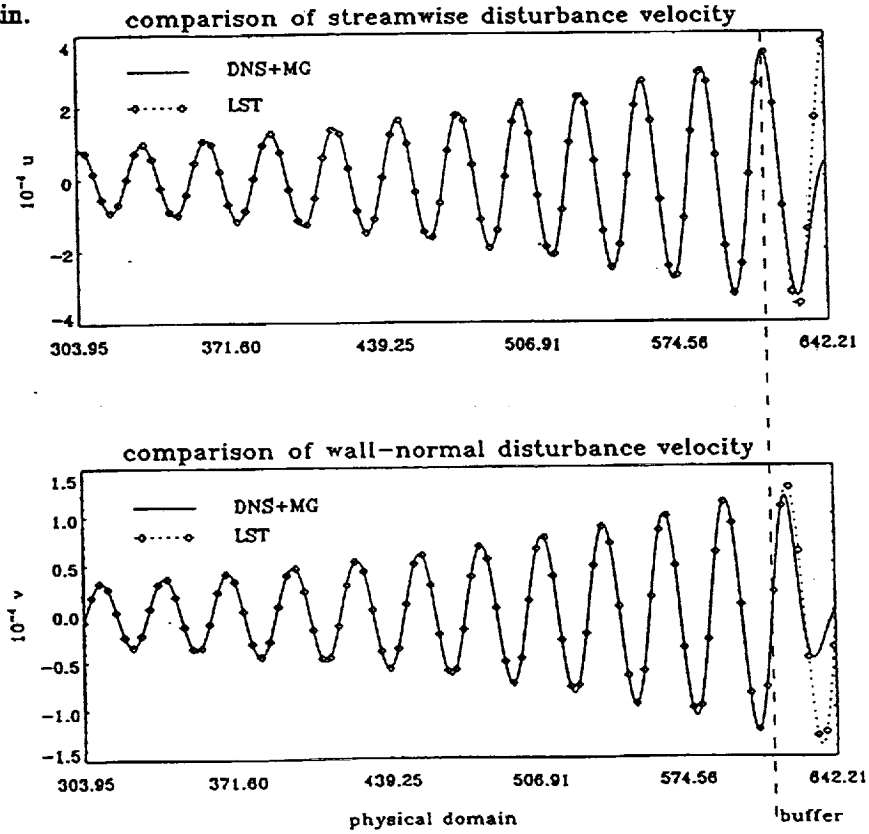

Figure 20. Comparison of the numerical and theoretical velocity components near the solid wall ($y^* = 1.3137$ for u and $y^* = 1.2448$ for v). $Re^* = 900$, $Fr = 86$, parallel wall-bounded base flow assumption is used grids: 362×50 (11 T-S wavelength physical domain + 1 wavelength buffer domain).

To compare our numerical results with those obtained by LST more precisely, we check the profiles of different Fourier modes.

The profiles of the disturbance waves are obtained by using the Fourier transformation. Generally, we can expand any continuous function in the spectral space. Since

$$\hat{u}(k) = \frac{\omega}{2\pi} \int_t^{t+T} \tilde{u}(x, y, t) e^{ik\omega t} dt, \tag{84}$$

where $\tilde{u}(x, y, t)$ is the complex disturbance velocity and $\hat{u}(k)$ are the Fourier coefficients corresponding to the frequency $k\omega$, we can then obtain

$$|\hat{u}(k)| = 2\sqrt{a(k)^2 + b(k)^2}, \quad k = 0, 1, 2, \cdots \tag{85}$$

with

$$a(k) = \frac{\omega}{2\pi} \int_t^{t+T} Real\{\tilde{u}(x, y, t)\} cos(k\omega t) dt, \tag{86}$$

$$b(k) = \frac{\omega}{2\pi} \int_t^{t+T} Real\{\tilde{u}(x, y, t)\} sin(k\omega t) dt. \tag{87}$$

Only the fundamental wave ($k = 1$) is obtained in this case. Figure 21 depicts the streamwise and wall-normal disturbance velocity profiles at $x^* = 439.2$ and 608.4 ($x^* = x/\delta^*_{x_0}$), and shows the excellent agreement with those obtained by linear stability theory.

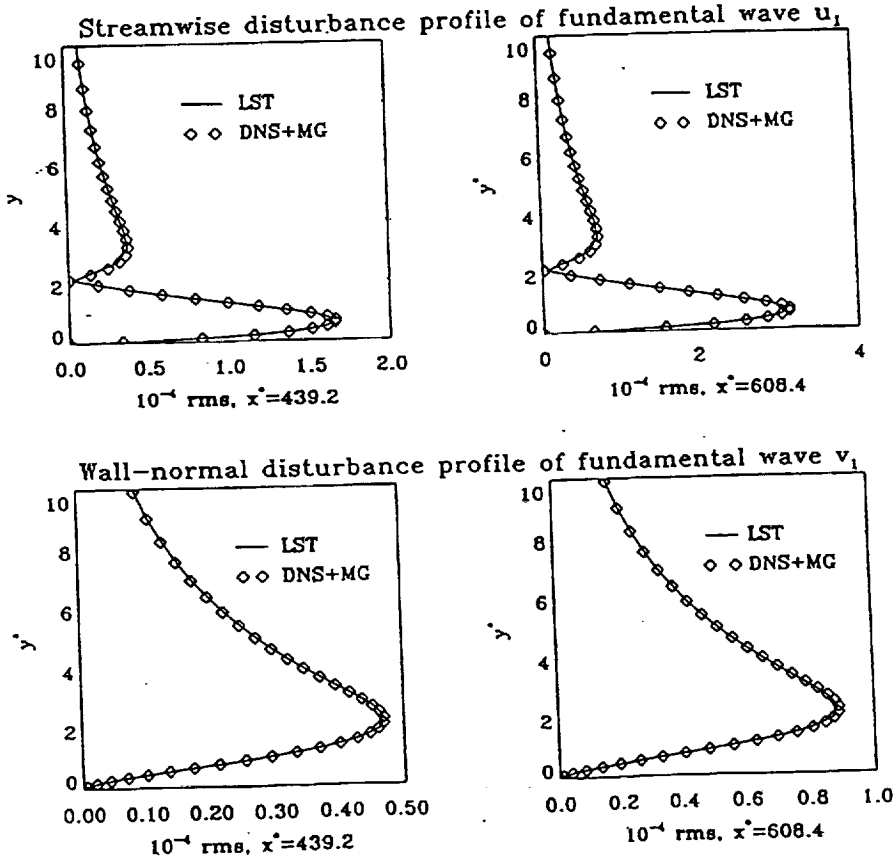

Figure 21. Comparison of the numerical and LST velocity profiles at $x^* = 439.2$ and 608.4.

To check the high order accuracy, two different grids (362×50 and 182×26) are tested. For this kind of unsteady problem, it is quite difficult to show the grid convergence. We define the relative L_2 error norm for both

u and v as

$$||E_u||_2 = \sqrt{\frac{\sum(u-u_e)^2}{\sum u_e^2}},$$

$$||E_v||_2 = \sqrt{\frac{\sum(v-v_e)^2}{\sum v_e^2}},$$

where u, v denote the numerical solution, and u_e, v_e denote the LST solution. The results given in Table I show that the accuracy of our scheme under the above measure is about $O(h^{3.5})$.

grids	$\|\|E_u\|\|_2$	$\|\|E_v\|\|_2$
182×26	0.3315	0.3243
362×50	0.0393	0.0319

Table I. Relative L_2 error norm for u and v after 13 T-S periods (calculated in physical domain).

10.2 Secondary instability and transition

Now we return to the real world. The base flow is now not parallel to the solid wall, but the Blasius similarity solution.

The computational domain is restricted to

$$\begin{aligned} x &\in [x_0, x_0 + l_x\lambda_0], \\ y &\in [0, y_{max}], \\ z &\in [\frac{\pi}{\beta|}, \frac{3\pi}{|\beta|}], \end{aligned}$$

where l_x is the number of T-S wavelengths in the computational domain, and λ_0 is the T-S wavelength at inflow (the T-S wavelength λ varies when the base flow is non-parallel).

A Benney-Lin (1960) type disturbance is imposed on the inflow:

$$\vec{v}(0,y,z,t) = \text{Real}\{\epsilon_{2d}\phi_{2d}^{(k)}(y)e^{i\omega t} + \epsilon_{3d+}\phi_{3d+}^{(k)}e^{i\omega t+i\beta x} + \epsilon_{3d-}\phi_{3d-}^{(k)}e^{i\omega t-i\beta x}\},$$

where $\phi_{2d}(y)$ and $\phi_{3d\pm}(y)$ correspond respectively to 2-D and 3-D eignsolutions of the Orr-Sommerfeld equation and the superscript (k) denotes different velocity components. Following is a typical case we chose:

$$\begin{aligned} Re_0^* &= 900, \quad Fr = 86 \ (\omega = 0.0774), \\ \beta &= 0.1, \quad y_{max} = 50, \\ \alpha_{2d} &= 0.2229 - 0.00451i, \\ \alpha_{3d} &= 0.2169 - 0.00419i, \\ \epsilon_{2d} &= 0.03, \quad \epsilon_{3d\pm} = 0.01, \\ l_x &= 10 \quad \text{with 2 T-S wavelengths for buffer domain} \\ x_0 &= 303.9, \quad x_{end} = 593.6. \end{aligned}$$

The grid we used here is $162 \times 34 \times 34$ (including eight wavelengths and a two wavelength buffer domain). The time step is set to $\frac{1}{280}$ of the 3-D T-S wave period.

It takes around 9 CRAY-YMP CPU hours for the code to run 30 T-S periods. Figures 22 and 23 depict the contours of relative helicity at different times which clearly show the process of K-type fundamental transition, λ-wave formation, the peak and valley splitting and vortex breakdown. It is found that the breakdown begins at the second peak when the λ-wave is intensified to certain degree and the shear flow is developed. The vortex breakdown further contaminates the flow field which leads to a transition process. The patterns of helicity at $t = 30T$ is very similar to those $t = 7T$, which suggests that the whole process of transition has been built up after $t = 7T$. It turns out that less than 2 CRAY-YMP hours are needed to simulate the whole process of transition for a $162 \times 34 \times 34$ grid and 7 T-S periods. Figures 24 and 25 give the contour plots of total vorticity magnitude on

the $y = 0.0477$ (x, z)-plane and spanwise vorticity on the $z = 31.4$ (x, y)-plane at different times which clearly show the process of vortex breakdown and formation of multiple spikes. The appearance of random moving small vortexes after breakdown provides a clue that the flow no longer keeps its laminar status. These contours also show a qualitative agreement with the laboratory experiment conducted by Saric et al. (1984).

The x-component of perturbation velocity, u, at different streamwise positions, $x = 305, 421$, and 537, but with same y-coordinate ($y = 0.3667$) is shown in Figure 26. Although the disturbance imposed at inflow is a sine function as shown at $x = 305$, the perturbation at other points is largely amplified and distorted. The perturbation velocity no longer keeps its sine function shape, but starts oscillating very fast, showing that high frequency modes have been induced.

We also averaged u and v on $z = 31.4$ (x, y)-plane at different streamwise positions, $x = 305, 363, 421, 479$, and 537 after the transition process was built up. The time-averaged $\bar{u}$ and $\bar{v}$ are given in Figures 27, 28, 29, and 30. Figures 28 and 29 depict the differences in $\bar{u}$ profiles between the Blasius similarity solution and computational results at $x = 421$ and 537, which qualitatively agree with the experimental results given by Suder, O'Brien, and Reshotko. Figures 28 and 29 also show that the $\bar{u}$-profile in the transition zone is sharper than those of Blasius solution. The wall stress $\tau = \mu \frac{\partial u}{\partial y}$ is then larger than that of laminar flows.

Figure 30 gives the $\bar{v}$-profile. The $\bar{v}$ is always positive in a laminar boundary layer. But, our computational results show that $\bar{v}$ varies from positive to negative and then becomes positive again. This is a typical sign that the flow is experiencing transition. Figure 31 shows that the spectrum of perturbation u becomes wider as the flow moves downstream. We also tried another case :

$$
\begin{aligned}
Re_0^* &= 732, \\
\omega_{2d} &= 0.0909, \\
\omega_{3d} &= 0.04545, \\
\beta &= 0.2418, \quad y_{max} = 50, \\
\alpha_{2d} &= 0.2490 - 0.00351i, \\
\alpha_{3d} &= 0.1103 - 0.00650i, \\
\epsilon_{2d} &= 0.015, \quad \epsilon_{3d\pm} = 0.005, \\
l_x &= 10 \quad \text{with 2 T-S wavelengths for buffer domain} \\
x_0 &= 248.2, \quad x_{end} = 437.5.
\end{aligned}
$$

The grid we used here is still $162 \times 34 \times 34$ (including eight wavelengths and a two wavelength buffer domain). This was set to correspond to a subharmonic transition, but we still got a k-type fundamental transition when we chose $\epsilon_{2d} = 0.03$ and $\epsilon_{3d\pm} = 0.01$. However, when we changed to $\epsilon_{2d} = 0.015$ and $\epsilon_{3d\pm} = 0.005$, a subharmonic transition was very clearly observed (see figure 32).

There is really a lack of reliable experimental data for transitional flow, which can be used to judge the computational results. Also, we need finer grids to get better resolution for post-onset flow or turbulent flow. We have to sacrifice those small eddies now. However, the results apparently provide physically correct simulations for the whole process of flow transition.

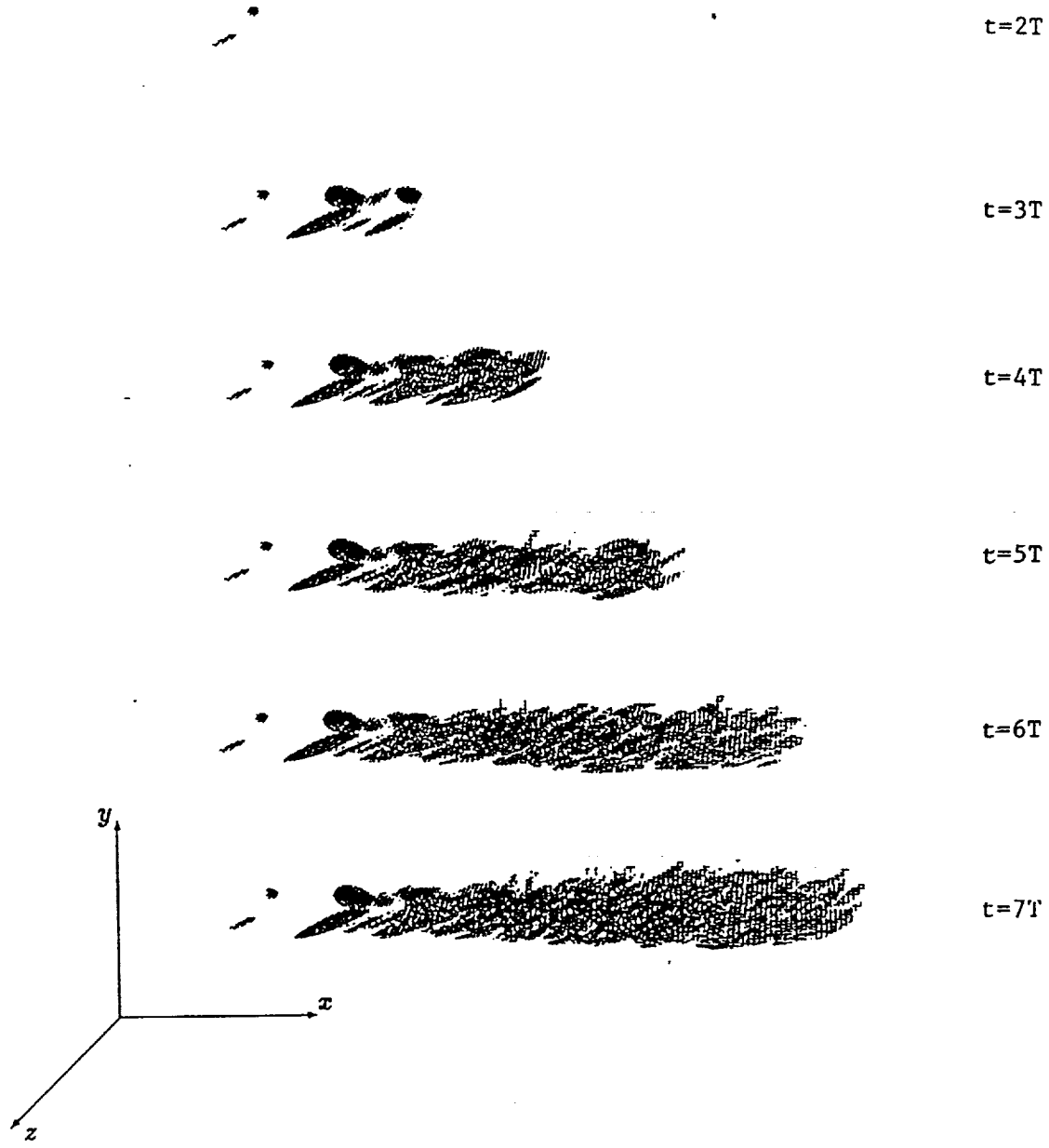

Figure 22. Front view of the relative helicity obtained on a $162 \times 34 \times 34$ gird at different times. $Re^* = 900, Fr = 86, \beta = 0.1, \epsilon_{2d} = 0.03, \epsilon_{3d} = 0.01$. Flow direction is from left to right.

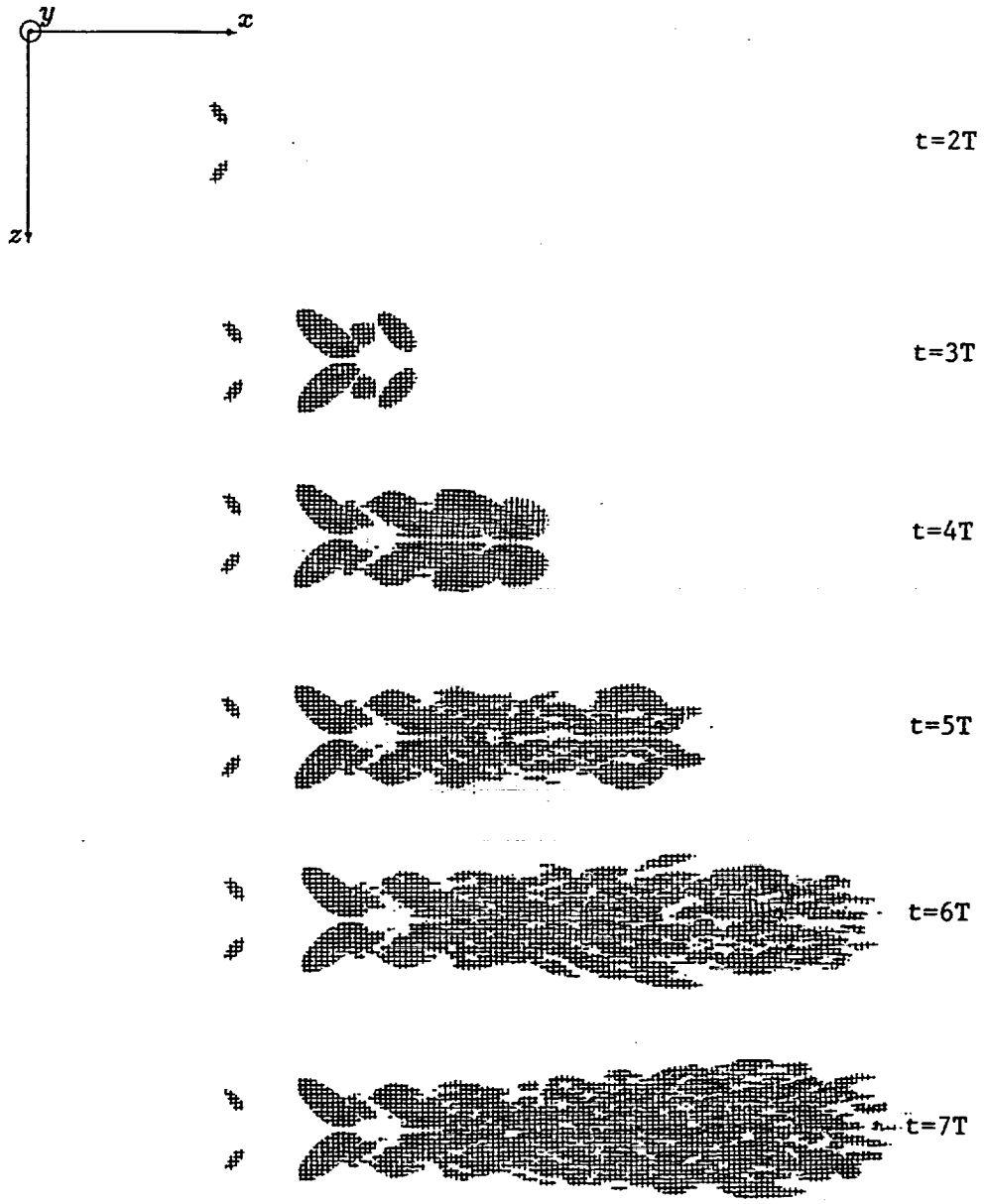

Figure 23. Bird view of the relative helicity obtained on a $162 \times 34 \times 34$ gird at different times. $Re^* = 900, Fr = 86, \beta = 0.1, \epsilon_{2d} = 0.03, \epsilon_{3d} = 0.01$. Flow direction is from left to right.

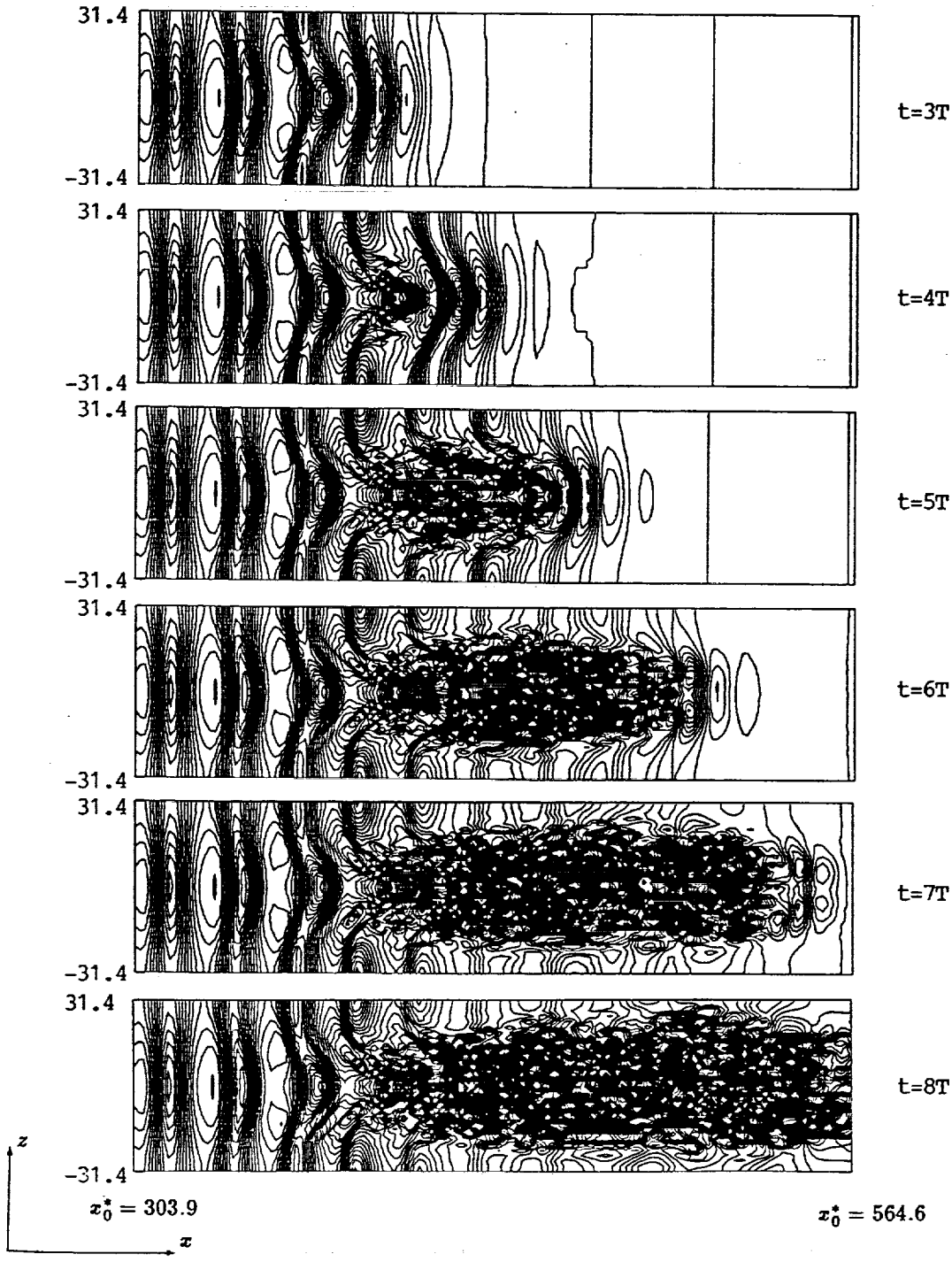

Figure 24. Contour plots of the total vorticity magnitude obtained on a $162 \times 34 \times 34$ gird at different times on the $y_0^* = 0.1123$ $(x, z)-$plane. $Re^* = 900, Fr = 86, \beta = 0.1$, $\epsilon_{2d} = 0.03, \epsilon_{3d} = 0.01$. Contour interval is 0.02, flow direction is from left to right.

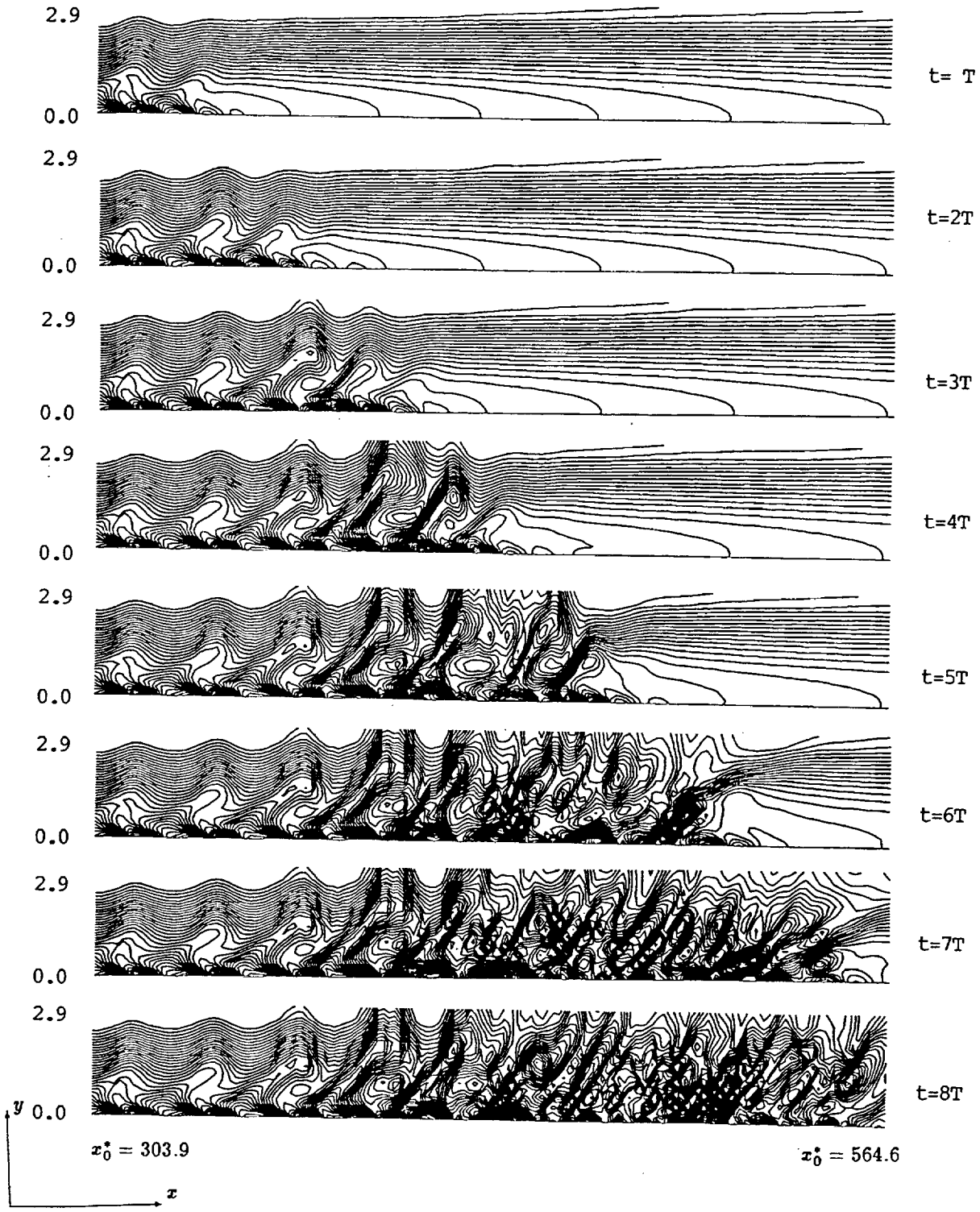

Figure 25. Contours plots of spanwise vorticity on the $z_0^* = 0$ (x, y)-plane at different times. $Re^* = 900, Fr = 86, \beta = 0.1, \epsilon_{2d} = 0.03, \epsilon_{3d} = 0.01$. Contour interval is 0.02, flow direction is from left to right.

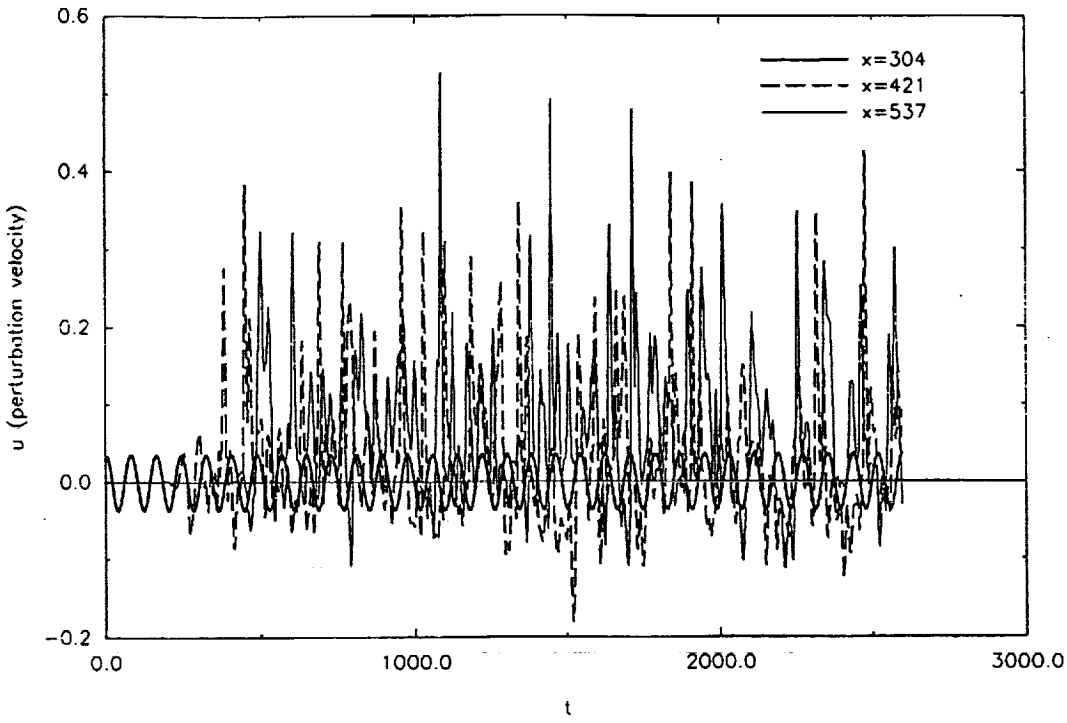

Figure 26. Temporal distribution of the perturbation velocity u on $y = 0.367, x = 304, 421$, and 537. $Re_0^* = 900, Fr = 86, \beta = 0.1, \epsilon_{2d} = 0.03, \epsilon_{3d} = 0.015$.

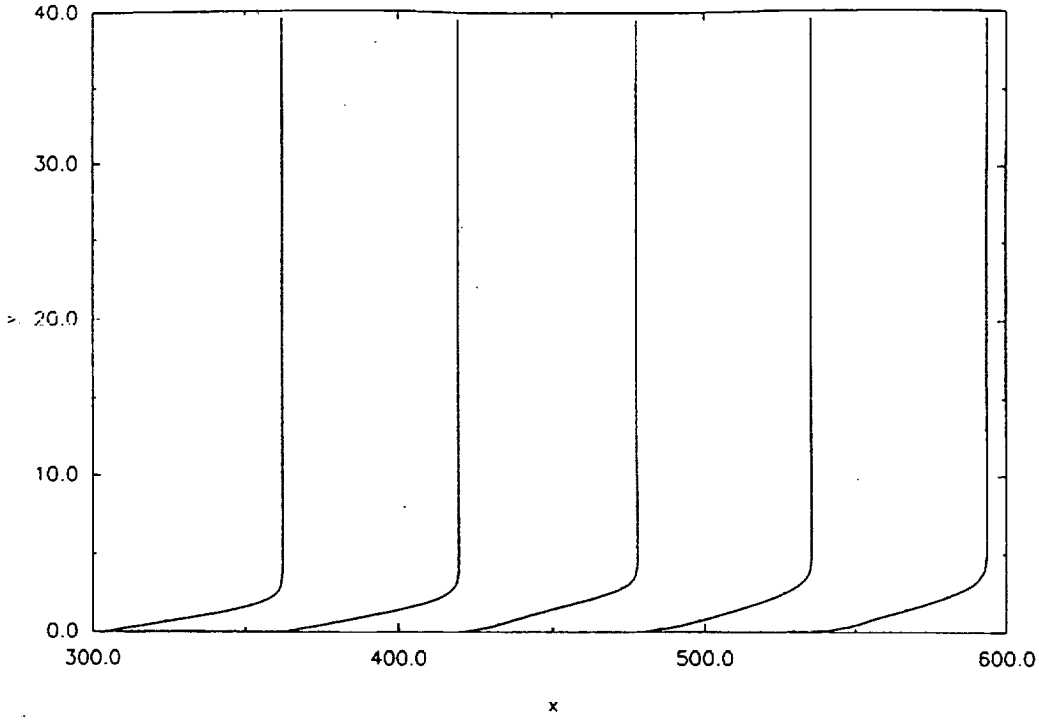

Figure 27. Time-averaged $\bar{u}$-profiles at $z = 31, x = 304, 362, 421, 479$, and 537. $Re_0^* = 900, Fr = 86, \beta = 0.1, \epsilon_{2d} = 0.03, \epsilon_{3d} = 0.01$.

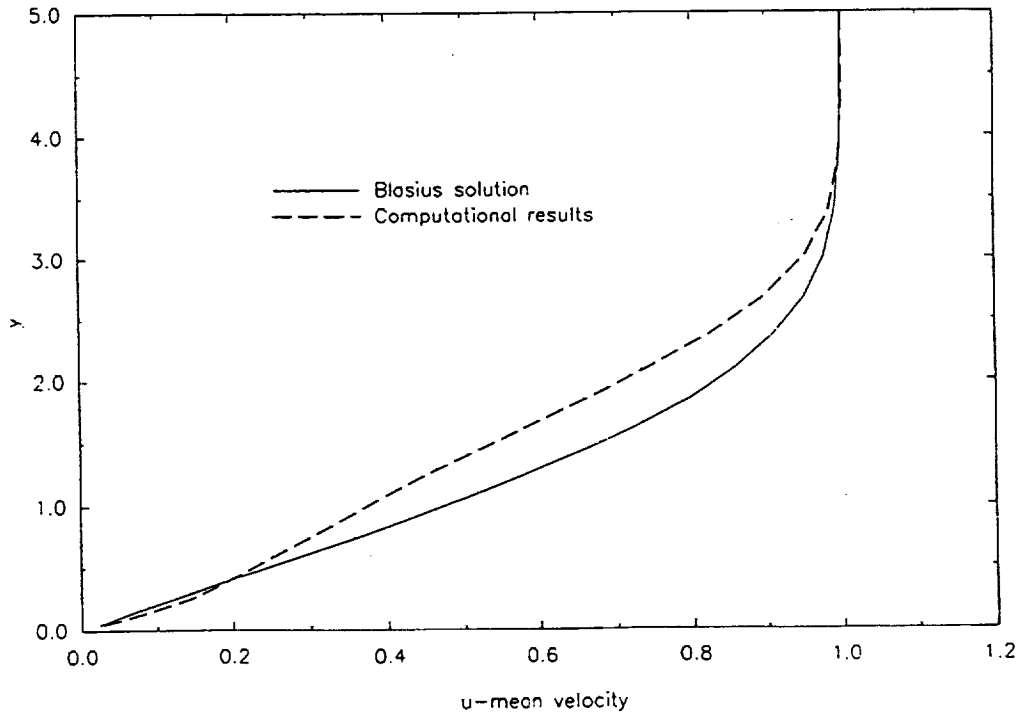

Figure 28. Comparison between $\bar{u}$-profiles and the Blasius profile at $x = 421, z = 31$. $Re_0^* = 900, Fr = 86, \beta = 0.1, \epsilon_{2d} = 0.03, \epsilon_{3d} = 0.01$.

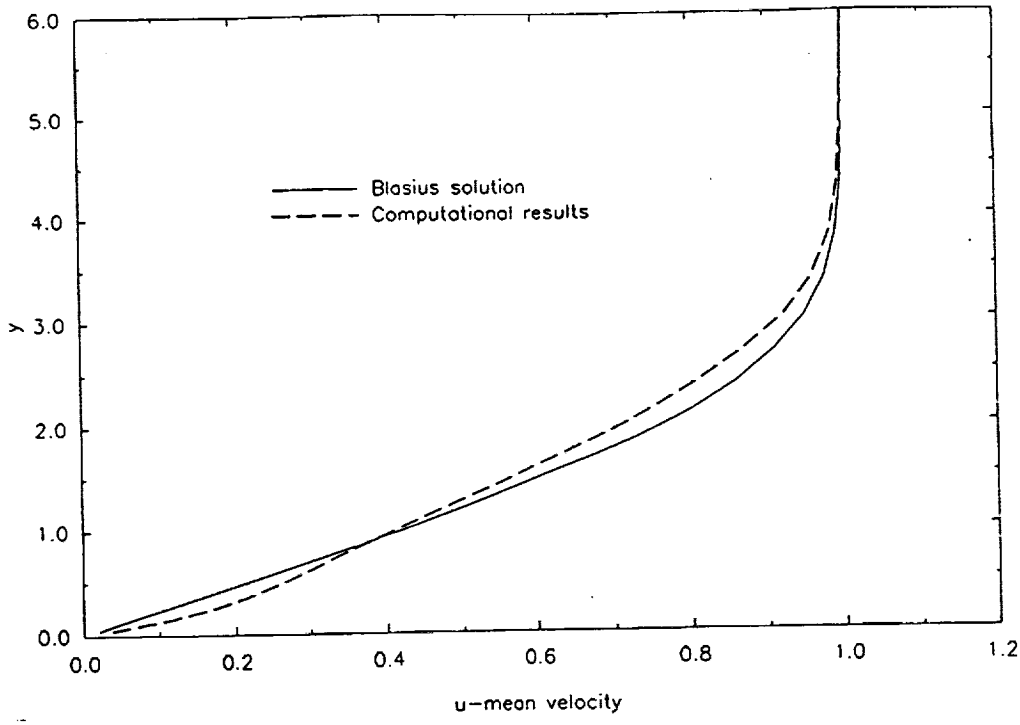

Figure 29. Comparison between $\bar{u}$-profile and the Blasius profile at $x = 537, z = 31$. $Re_0^* = 900, Fr = 86, \beta = 0.1, \epsilon_{2d} = 0.03, \epsilon_{3d} = 0.01$.

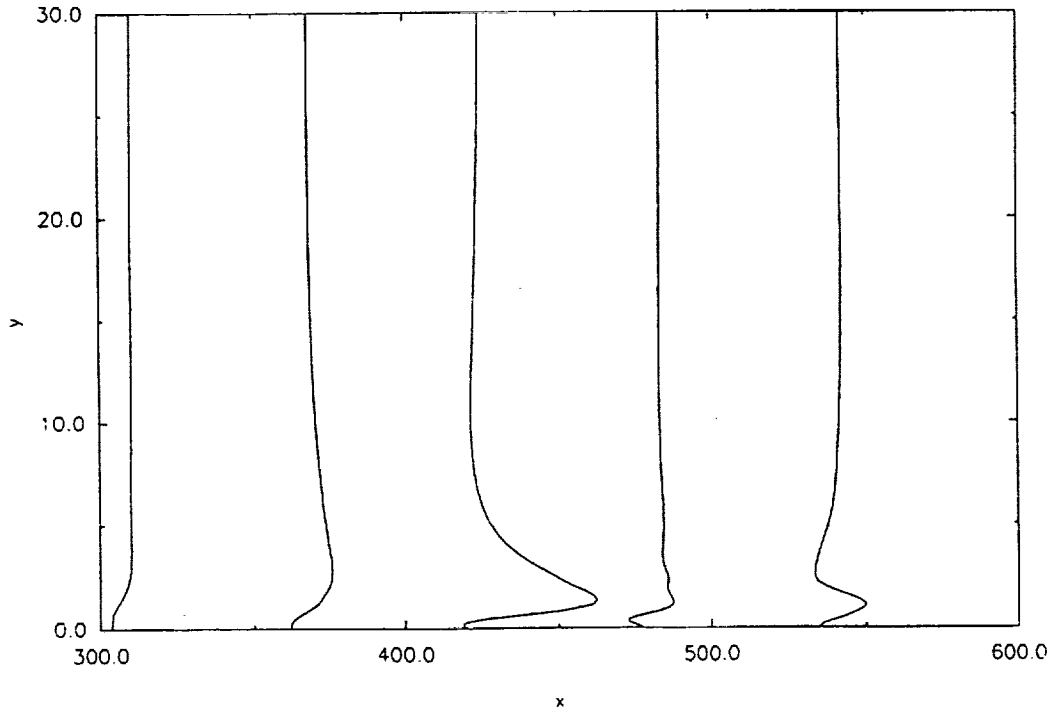

Figure 30. Time-averaged $\bar{v}$-profiles at $z = 31, x = 304, 362, 421, 479$, and 537. $Re_0^* = 900, Fr = 86, \beta = 0.1, \epsilon_{2d} = 0.03, \epsilon_{3d} = 0.01$.

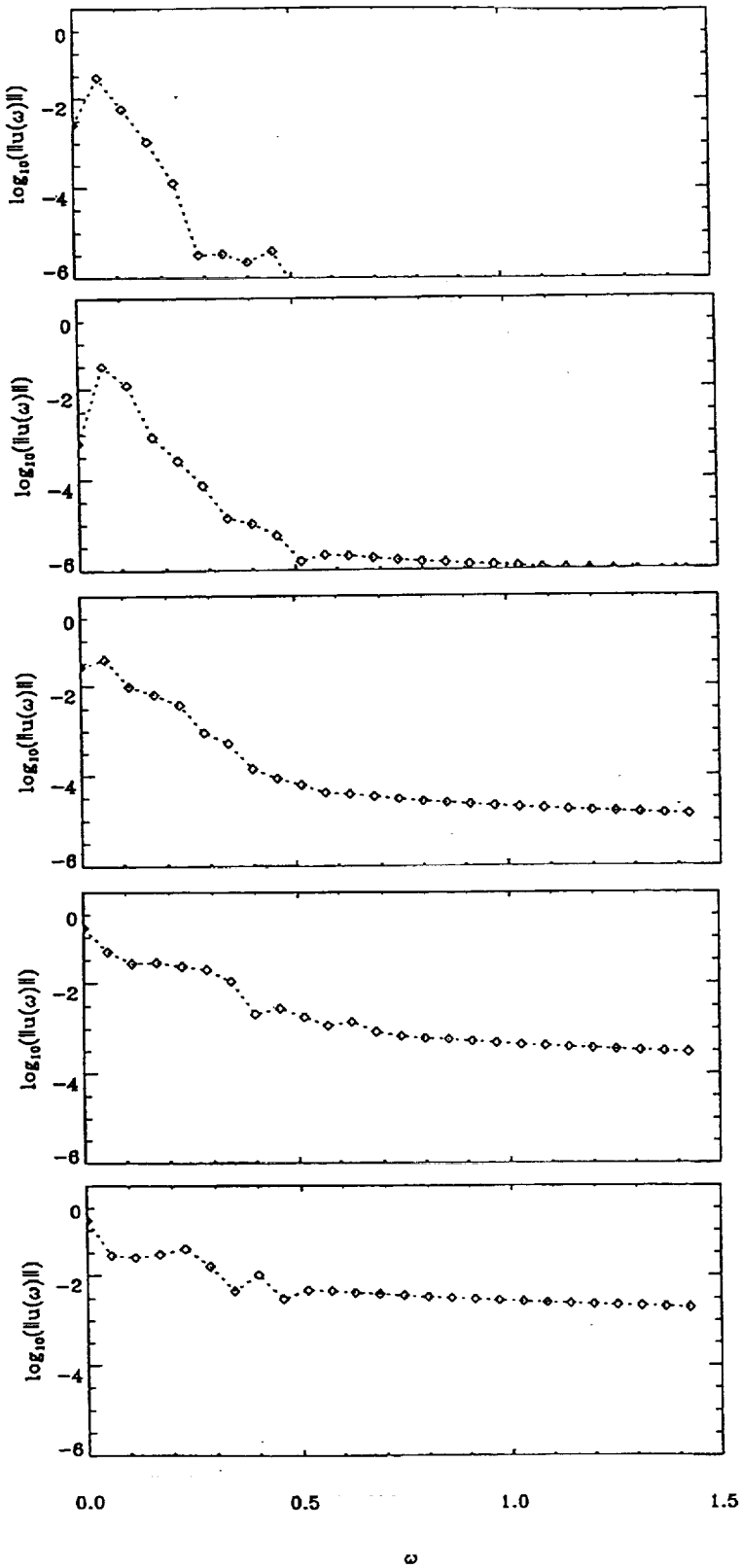

Figure 31. Streamwise distribution of the $\bar{u}$-spectrum at $y = 0.715, x = 319.3, 362.8, 406.2, 449.7,$ and 478.6 $Re_0^* = 900, Fr = 86, \beta = 0.1, \epsilon_{2d} = 0.03, \epsilon_{3d} = 0.01$i, and a $114 \times 34 \times 18$ grid (6 T-S wavelengths physical domain +1 wavelength buffer) is used.

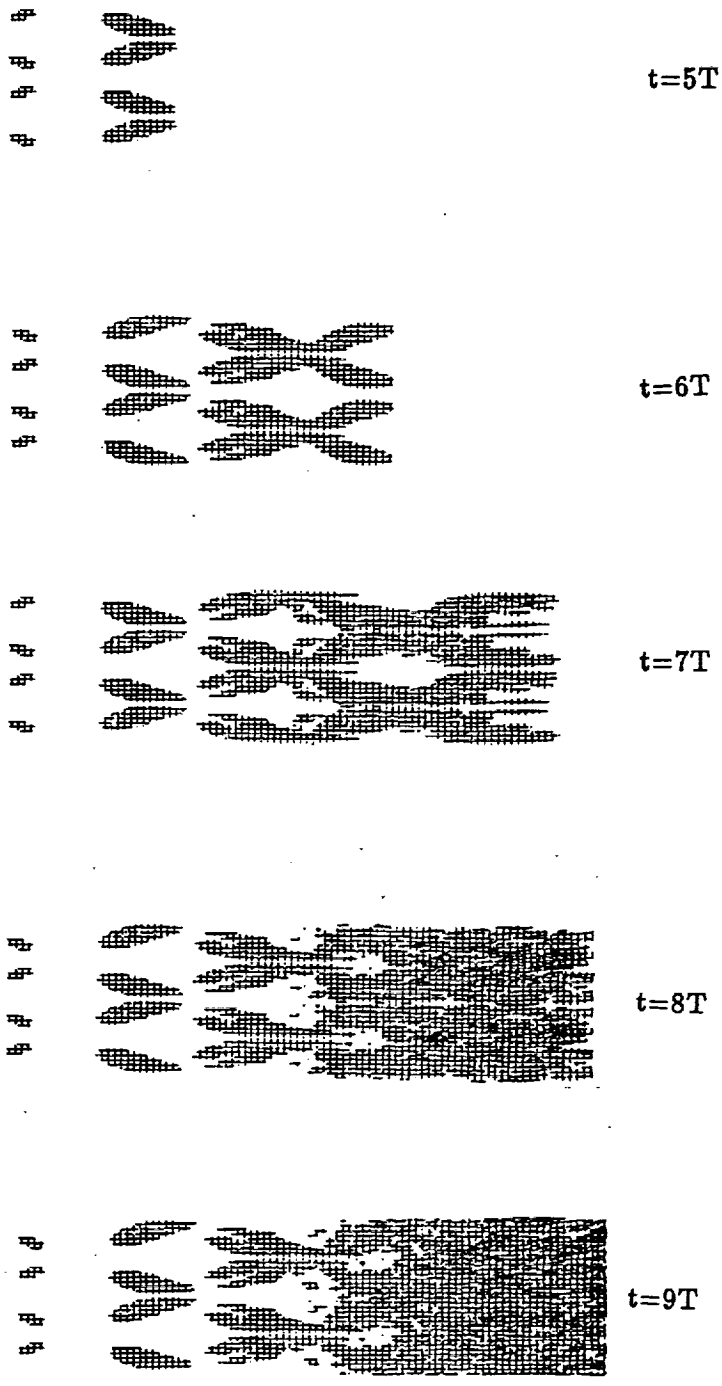

Figure 32. Bird view of the relative helicity of subharmonic transition obtained on a $162 \times 34 \times 34$ gird at different times. $Re^* = 732, \beta = 0.2418, \epsilon_{2d} = 0.015, \epsilon_{3d} = 0.005$. Flow direction is from left to right.

11 Concluding Remarks

- The fully implicit time-marching and fourth-order finite difference scheme on a stretched and staggered grid is accurate enough to simulate the pre-onset transitional flow with a relatively coarse grid. The computational results agree with linear stability theory, secondary instability theory and some experiments.
- The simulation with relatively coarse grids still can provide qualitatively correct prediction for transitional flow. It shows that the large eddies play more important roles in the process of flow transition.
- The spatial DNS with relatively coarse grids meets trouble at the flow breakdown stage since the grid is not fine enough to resolve the small eddies which play the role to generate dissipations. We then need to introduce some numerical dissipation. The new fine-coarse-fine grid mapping technique can keep the DNS code running to simulate the whole process of transition, including the linear growth, secondary instability, breakdown, and transition.
- To get more accurate DNS simulations, we still need finer grids, especially for post-onset flows.

12 Acknowledgements

The authors thanks NASA Langley Research Center and NASA Lewis Research Center for the sponsorship. The authors also appreciate the very helpful discussions with Drs. T.H. Shih, Z.G. Yang, and A. Shabbir at ICOMP/NASA Lewis Research Center.

References

[1] Danabasoglu, G., Biringen,S. & Streett, C. L., 1991 'Numerical Simulation of Spatially Evolving Instability in Plane Channel Flow', *AIAA Paper No.* 91-0234.

[2] Fasel, H., 1976 'Investigation of the Stability of Boundary Layers by a Finite Difference Model of the Navier-Stokes Equations', *J. Fluid Mech.* **78**, 355.

[3] Fasel, H., & Bestek, H., 1980 'Investigation of Nonlinear, Spatial Disturbance Amplification on Plane Poiseuille Flow', in *Laminar-Turbulent Transition,* edited by R. Eppler & H. Fasel, 173-185, Springer-Verlag, Germany.

[4] Fasel, H., Rist, U. & Konzelmann, U., 1987 'Numerical Investigation of the Three-Dimensional Development in Boundary Layer Transition', *AIAA Paper No.* 87-1203.

[5] Fasel, H. & Konzelmann, U., 1990 'Nonparallel Stability of a Flat Boundary Layer Using the Complete Navier-Stokes Equations', *J. Fluid Mech.* **221**, 311.

[6] Herbert, Th., 1983a 'Secondary Instability of Plane Channel Flow to Subharmonic Three-Dimensional Disturbances', *Phys, Fluids* **26**, 871.

[7] Herbert, Th., 1983b 'Subharmonic Three-Dimensional Disturbances in Unstable Plane Shear Flow', *AIAA Paper No.* 83-1759.

[8] Joslin, R., Streett, C., and Chang, C., 1992 'Validation of Three-Dimensional Incompressible Spatial Direct Numerical Simulation Code – A Comparison with Linear Stability and Parabolic Stability Equation Theories for Boundary-Layer Transition on a Flat Plate', *NASA Technical Paper* 3205.

[9] Kachanov, Y. S., Kozlov, V. V. & Levchenko, V. Y., 1978 'Nonlinear Development of a Wave in a Boundary Layer', *Fluid Dynamics* **12**, 383.

[10] Klebanoff, P. S., Tidstrom, K. D., & Sargent, 1962 'The Three-Dimensional Nature of Boundary Layer Instability', *J. Fluid Mech.* **12**, 1.

[11] Kleiser, L., & Laurien, E., 1985 'Numerical Investigation of Interactive Transition Control', *AIAA Paper No.*85-0566.

[12] Kleiser, L. & Zang, T. A., 1991 'Numerical Simulation of Transition in Wall Bounded Shear Flow', *Ann. Rev. Fluid Mech.* **23**, 495.

[13] Orr, William M'F., 1907a 'The Stability or Instability of the Steady Motions of a Perfect Liquid and of a Viscous Liquid. Part I.: A Perfect Liquid', *Proc. Royal Irish Acad.,* Vol. 27, Section A, No.2, 9-68.

[14] Orr, William M'F., 1907b 'The Stability or Instability of the Steady Motions of a Liquid. Part II.: A Viscous Liquid', *Proc. Royal Irish Acad.*, Vol. 27, Section A, No.3, 69-138.

[15] Orszag, S. A. & Kells, L. C., 1980 'Transition to Turbulence in Plane Poiseuille Flow and Plane Couette Flow', *J. Fluid Mech.* **96**, 159.

[16] Saric, W. S., Kozlov, V. V. & Levchenko, C. Ya, 1984 'Forced and Unforced Subharmonic Resonance in Boundary-Layer Transition', *AIAA Paper No.* 84-0007.

[17] Schlichting, H., 1932 'Uber die Entstehung der Turbulenz in Einem Rotierenden Zylinder', *Math-Phys. KL.*, No. 2, 160-198.

[18] Schubauer, G. B. & Skramstad, H. K., 1948 'Laminar-Boundary-Layer Oscillations and Transition on a Flat Plate', *NACA Rep.* 909.

[19] Sommerfeld, A., 1908 'Ein Beitrag zur Hydrodynamischen Erklaerung der Turbulenten Fluessigkeitsbewegungen', *Atti del 4.* Congressio Internazionale dei Matimatica III (Rome), 116-124.

[20] Suder, K.L., O'Brien, J.E., & Reshotko, E., 1988 'Experimental study of bypass transition in a boundary layer', *NASA TM* **100913**.

[21] Spalart, P. R., 1989 'Direct Numerical Study of Leading-Edge Contamination', *Fluid Dynamics of Three-Dimensional Turbulent Shear Flows and Transition,* AGARD-CP-438, 5.1-5.13.

[22] Tollmien, W. (Dwight M. Miner, transl.) 1931 'The Production of Turbulence', NACA TM 609.

[23] Wray, A., & Hussaini. M. Y., 1984 'Numerical Experiments in Boundary Layer Stability', *Proc. R. Soc. Lond. A 392*, 373.

[24] Zang, T.A. & Hussaini, M.Y., 1986 'On Spectral Multigrid Methods for the Time-dependent Navier-Stokes Equations', *Appl. Math. Comput.* **19**, 359–372.

[25] Zang, T. A., Krist, S. E., Erlebacher, G., & Hussaini, M. Y., 1987 'Nonlinear Structures in the Later Stages of Transition', *AIAA Paper No.* 87-1204.

REPORT DOCUMENTATION PAGE

Form Approved
OMB No. 0704-0188

Public reporting burden for this collection of information is estimated to average 1 hour per response, including the time for reviewing instructions, searching existing data sources, gathering and maintaining the data needed, and completing and reviewing the collection of information. Send comments regarding this burden estimate or any other aspect of this collection of information, including suggestions for reducing this burden, to Washington Headquarters Services, Directorate for Information Operations and Reports, 1215 Jefferson Davis Highway, Suite 1204, Arlington, VA 22202-4302, and to the Office of Management and Budget, Paperwork Reduction Project (0704-0188), Washington, DC 20503.

1. AGENCY USE ONLY (Leave blank)	2. REPORT DATE	3. REPORT TYPE AND DATES COVERED
	November 1993	Technical Memorandum

4. TITLE AND SUBTITLE

Multigrid Direct Numerical Simulation of the Whole Process of Flow Transition in 3–D Boundary Layers

5. FUNDING NUMBERS

WU–505–90–5K

6. AUTHOR(S)

Chaoqun Liu and Zhining Liu

7. PERFORMING ORGANIZATION NAME(S) AND ADDRESS(ES)

National Aeronautics and Space Administration
Lewis Research Center
Cleveland, Ohio 44135–3191

8. PERFORMING ORGANIZATION REPORT NUMBER

E–8175

9. SPONSORING/MONITORING AGENCY NAME(S) AND ADDRESS(ES)

National Aeronautics and Space Administration
Washington, D.C. 20546–0001

10. SPONSORING/MONITORING AGENCY REPORT NUMBER

NASA TM–106369
ICOMP–93–36;
CMOTT–93–13

11. SUPPLEMENTARY NOTES

Chaoqun Liu, Institute for Computational Mechanics in Propulsion and Center for Modeling of Turbulence and Transition, NASA Lewis Research and University of Colorado at Denver, Denver, Colorado 80217; and Zhining Liu, Center for Computational Mathematics, CU Denver, University of Colorado at Denver, Denver, Colorado, 80217, (work funded under NASA Cooperative Agreement NCC3–233). This work was also supported by NASA Langley Research Center under grant number NAS1–10312. ICOMP Program Director, Louis A. Povinelli, (216) 433–5818.

12a. DISTRIBUTION/AVAILABILITY STATEMENT

Unclassified - Unlimited
Subject Category 34

12b. DISTRIBUTION CODE

13. ABSTRACT ***(Maximum 200 words)***

A new technology was developed in this study which provides a successful numerical simulation of the whole process of flow transition in 3-D boundary layers, including linear growth, secondary instability, breakdown, and transition at relatively low CPU cost. Most other spatial numerical simulations require high CPU cost and blow up at the stage of flow breakdown. A fourth-order finite difference scheme on stretched and staggered grids, a fully implicit time-marching technique, a semi-coarsening multigrid based on the so-called approximate line-box relaxation, and a buffer domain for the outflow boundary conditions were all used for high-order accuracy, good stability, and fast convergence. A new fine-coarse-fine grid mapping technique was developed to keep the code running after the laminar flow breaks down. The computational results are in good agreement with linear stability theory, secondary instability theory, and some experiments. The cost for a typical case with $162 \times 34 \times 34$ grid is around 2 CRAY-YMP CPU hours for 10 T-S periods.

14. SUBJECT TERMS

Transition; Boundary layers; Multigrid; Secondary instability; Spatial direct numerical simulation

15. NUMBER OF PAGES

40

16. PRICE CODE

A03

17. SECURITY CLASSIFICATION OF REPORT	18. SECURITY CLASSIFICATION OF THIS PAGE	19. SECURITY CLASSIFICATION OF ABSTRACT	20. LIMITATION OF ABSTRACT
Unclassified	Unclassified	Unclassified	